DFTT 34/95
DTP/96/100
Cavendish-HEP-96/20
ETH-TH-96/48
November 1996

Higgs Production at the LHC: an Update on Cross Sections and Branching Ratios[1]

Z. Kunszt[a], S. Moretti[b,c] and W. J. Stirling[d,e]

a) Theoretical Physics, ETH, Zürich, Switzerland.

b) Dipartimento di Fisica Teorica, Università di Torino, and I.N.F.N., Sezione di Torino, Via Pietro Giuria 1, 10125 Torino, Italy.

c) Cavendish Laboratory, University of Cambridge, Madingley Road, Cambridge, CB3 0HE, United Kingdom.

d) Department of Physics, University of Durham, South Road, Durham DH1 3LE, United Kingdom.

e) Department of Mathematical Sciences, University of Durham, South Road, Durham DH1 3LE, United Kingdom.

Abstract

New theoretical and experimental information motivates a re-examination of the Standard Model Higgs production rates at the LHC pp collider. We present calculations of the relevant cross sections and branching ratios, including recently calculated QCD next-to-leading order corrections, new parton distributions fitted to recent HERA structure function data, and new values for electroweak input parameters, in particular for the top quark mass. Cross sections are calculated at two collider energies, $\sqrt{s} = 10$ TeV and 14 TeV.

[1]Work supported in part by Ministero dell' Università e della Ricerca Scientifica.

E-mails: Kunszt@itp.phys.ethz.ch; Moretti@hep.phy.cam.ac.uk; W.J.Stirling@durham.ac.uk.

1 Introduction

The discovery of the Standard Model ($\mathcal{SM}$) Higgs boson is one of the most important physics goals of the Large Hadron Collider (LHC). An important prerequisite of LHC Higgs phenomenology is a precise knowledge of the various production cross sections and decay branching ratios. Detailed studies (see, for example, Refs. [1, 2]) have shown that there is no single production mechanism or decay channel which dominates the phenomenology over the whole of the relevant Higgs mass range, $O(100 \text{ GeV}) < M_H < O(1 \text{ TeV})$, rather there are several different scenarios depending on the value of M_H.

The precision with which such calculations can be performed has improved significantly over the years. In particular,

(i) next-to-leading order corrections are now known for most of the subprocess production cross sections and partial decay widths;

(ii) knowledge of the parton distribution functions has improved as more precision deep inelastic and other data have become available;

(iii) the range of possible input parameter values (in particular the top quark mass m_t) has decreased as a result of precision measurements from LEP, the Tevatron $p\bar{p}$ collider and other experiments.

As a consequence, many of the numerical results to be found in the literature are now out-of-date. We are therefore motivated to update the calculations [3] of the relevant cross sections and branching ratios to take into account the improvements discussed above. The output of our analysis will be a set of benchmark results for cross sections and event rates as a function of M_H, for the two 'standard' LHC collision energies, $\sqrt{s} = 10$ and 14 TeV. Note that we are not attempting to perform a detailed analysis of signals, backgrounds and search strategies. In this respect, by far the most complete studies to date can be found in the recent ATLAS [4] and CMS [5] Technical Proposals. Even there, however, one finds slight inconsistencies in the way the cross sections and branching ratios are calculated (leading versus next-to-leading order cross sections, out-of-date parton distributions and parameter values, etc.). The present study will enable the Higgs production cross sections, event rates and significance factors used in Refs. [4] and [5] to be renormalised to the most up-to-date values.

Another important factor is the theoretical uncertainty of the predictions. In most cases we can estimate these by varying appropriate input quantities like the parton distributions, parameter values and renormalisation and factorisation scales. As a result, we can identify those quantities where more theoretical work is needed to improve the precision.

The paper is organised as follows. In the following Section we list and discuss the set of QCD and electroweak input parameters for the calculations. In Section 3 we calculate the complete set of branching ratios needed to predict event rates for specific channels. Section 4 contains the main results of the paper: numerical cross section calculations for a variety of Higgs production and decay processes. Finally, our conclusions and outlook are presented in Section 5.

2 Electroweak and QCD input parameters

Most of the discrepancies in the literature concerning the values of Higgs cross sections and branching ratios arises simply from different choices of the electroweak and QCD input parameters. For reference, therefore, we list here the numerical values adopted in this study:

$$\begin{aligned} M_Z &= 91.186 \text{ GeV}, & \Gamma_Z &= 2.495 \text{ GeV}, \\ M_W &= 80.356 \text{ GeV}, & \Gamma_W &= 2.088 \text{ GeV}, \\ G_F &= 1.16639 \times 10^{-5} \text{ GeV}^{-2}, & \alpha_{em} &\equiv \alpha_{em}(M_Z) = 1/128.9. \end{aligned} \tag{1}$$

Although each of these parameters has a small measurement error, the effect of these on the event rates computed below is negligible compared to other uncertainties. The charged and neutral weak fermion–boson couplings are defined by

$$g_W^2 = \frac{e^2}{\sin^2\theta_W} = 4\sqrt{2} G_F M_W^2, \qquad g_Z^2 = \frac{e^2}{\sin^2\theta_W \ \cos^2\theta_W} = 4\sqrt{2} G_F M_Z^2. \tag{2}$$

For the vector and axial couplings of the Z boson to fermions, we use the 'effective leptonic' value

$$\sin^2_{\rm eff}(\theta_W) = 0.232. \tag{3}$$

The QCD strong coupling enters explicitly in the production cross sections and in the branching ratios, and implicitly in the parton distributions. Since most quantities we calculate are known to next-to-leading order, unless otherwise stated we use α_s evaluated at two-loop order, with[2] $\Lambda_{\overline{MS}}^{(4)} = 230$ MeV to match our default parton

[2]The values of $\Lambda_{\overline{MS}}^{(n_f)}$ for other n_f's are calculated according to the prescription in Ref. [6].

distribution set, and with a scale μ chosen appropriately for the process in question. The choice of scale for production cross sections is discussed in Section 4 below, while for the branching ratios we adopt the prescriptions of Refs. [7, 8, 9]. Our default parton distributions are the MRS(A) set [10], which have been fitted to a wide range of HERA and other deep inelastic scattering data. We also display results for the recent MRS(R1,R2) parton sets [11]. They represent an update of the MRS(A) set and are fitted to the latest HERA data. They also enable us to study the dependence of the production cross sections on the value of α_s in a consistent manner.[3]

For the fermion masses we take $m_\mu = 0.105$ GeV, $m_\tau = 1.78$ GeV, $m_s = 0.3$ GeV, $m_c = 1.4$ GeV, $m_b = 4.25$ GeV and $m_t = 175$ GeV, with all decay widths equal to zero except for Γ_t. We calculate this at tree-level within the $\mathcal{SM}$, using the expressions given in Ref. [12]. We study the variation of the production cross sections with m_t in the range $165 < m_t < 185$ GeV, which subsumes the recent direct measurement (CDF and D0 combined) from the Tevatron $p\bar{p}$ collider of $m_t = 175 \pm 6$ GeV [13]. The first generation of fermions and all neutrinos are taken to be massless, i.e. $m_u = m_d = m_e = m_{\nu_e} = 0$ and $m_{\nu_\mu} = m_{\nu_\tau} = 0$, with zero decay widths.

We assume that $M_H = 80$ GeV is a conservative discovery mass limit for LEP2, and therefore focus our attention on the mass range 80 GeV $\leq M_H \leq 1$ TeV. The discussion naturally falls into classes, depending on whether M_H is less than or greater than $O(2M_W)$[4].

3 $\mathcal{SM}$ Higgs branching ratios

The branching ratios of the $\mathcal{SM}$ Higgs boson have been studied in many papers. A useful compilation of the early works on this subject can be found in Ref. [1], where all the most relevant formulae for on-shell decays are summarised. Higher-order corrections to most of the decay processes have also been computed (for up-to-date reviews see Refs. [14, 15] and references therein), as well as the rates for the off-shell decays $H \to W^*W^*, Z^*Z^*$ [16], $H \to Z^*\gamma$ [17] and $H \to t^*\bar{t}^*$ [18]. Threshold effects due to the possible formation of $t\bar{t}$ bound states in the one-loop induced process $H \to \gamma\gamma$ have also been studied [19].

[3]When we compare the cross sections obtained by using different sets of parton distributions, we of course use the appropriate $\Lambda^{(n_f)}_{\overline{MS}}$ values.

[4]This defines the so-called 'intermediate-mass' and 'heavy' Higgs mass ranges, respectively.

In our calculations we include only the (large) QCD corrections to the $\mathcal{SM}$ Higgs partial widths into heavy quark pairs [7] and into $Z\gamma$, $\gamma\gamma$ [8] and gg [9][5]. Since the QCD corrections to the top loops in $Z\gamma$, $\gamma\gamma$ and gg decays, as given in Ref. [8], are valid only for $M_H \ll 2m_t$, we have implemented these only far below the $t\bar{t}$ threshold, which is in fact the only region where these decay channels could be important[6].

The bulk of the QCD corrections to $H \to q\bar{q}$ can be absorbed into a 'running' quark mass $m_q(\mu)$, evaluated at the energy scale $\mu = M_H$ (for example). The importance of this effect for the case $q = b$, with respect to intermediate-mass Higgs searches at the LHC, has been discussed in Ref. [3]. There is, however, a slight subtlety concerning $t\bar{t}$ decays [21]. For $H \to q\bar{q}$ decays involving light quarks ($q = s, c, b$), the use of the running quark mass $m_q(\mu = M_H)$ takes into account large logarithmic corrections at higher orders in QCD perturbation theory [7], and so in principle one could imagine using the same procedure for $H \to t\bar{t}$, at least in the limit $M_H \gg m_t$. In practice, however, we are interested only in the region $M_H/m_t \sim O(1)$. In the case of the top quark loop mediated decay $H \to gg$, it is well known that the higher-order QCD corrections are minimised if the quark mass is defined at the pole of the propagator, i.e. $m_t(\mu = m_t)$ [22]. To be consistent, therefore, we use the *same* top mass $m_t(\mu = m_t)$ in the decay width for $H \to t\bar{t}$ (and $H \to Z\gamma, \gamma\gamma$ as well). For the light quark loop contributions to the $H \to gg(Z\gamma, \gamma\gamma)$ decay widths we use pole(running) masses (defined at the scale $\mu = M_H$) [22, 23].

Our results on the Higgs branching ratios are summarised in Figs. 1–3. Fig. 1 shows the branching ratios, for $M_H \leq 200$ GeV, for the channels: (a) $b\bar{b}$, $c\bar{c}$, $\tau^+\tau^-$, $\mu^+\mu^-$ and gg; and (b) WW, ZZ, $\gamma\gamma$ and $Z\gamma$. The patterns of the various curves are not significantly different from those presented in Ref. [3]. The inclusion of the QCD corrections in the quark-loop induced decays (which apart from small changes in the parameter values is the only significant difference with respect to the calculation in [3]) turns out to give a variation of at most a few per cent for the decays $H \to \gamma\gamma$ and $H \to Z\gamma$, while for $H \to gg$ differences are of order 50–60%. However this has little phenomenological relevance, since this decay width makes a negligible contribution to the total width, and is an unobservable channel in practice.

Note that for the below-threshold decays $H \to W^*W^*$ and $H \to Z^*Z^*$, we do

[5]The higher-order electroweak corrections and their interplay with the QCD corrections do not significantly change the branching ratios which are phenomenologically relevant for Higgs searches at the LHC.

[6]Numerical results valid for any value of the ratio $\tau = M_H^2/4m_t^2$ have recently been presented [20].

not constrain one of the vector bosons to be on-shell when the decaying Higgs boson mass exceeds the gauge boson rest mass. Instead we integrate numerically over the virtualities of both decay products, see for example Ref. [21], thus avoiding errors in the threshold region.

Fig. 2 shows the $\mathcal{SM}$ Higgs branching ratios for 200 GeV $\leq M_H \leq$ 1000 GeV. Apart from our use of a different m_t value, the curves show the same distinctive features as those presented in Ref. [3]. The inclusion here of below-threshold $H \to t^* \bar{t}^*$ decays does not give any observable effect, since this channel is heavily suppressed by the WW and ZZ decays.

For completeness, we show in Fig. 3 the total $\mathcal{SM}$ Higgs decay width over the range 50 GeV $\leq M_H \leq$ 1000 GeV. For further comments on the implications of the various $\mathcal{SM}$ Higgs branching ratios on the various search strategies, we refer the reader to Ref. [3].

4 $\mathcal{SM}$ Higgs production cross sections and event rates

There are only a few Higgs production mechanisms which lead to detectable cross sections at the LHC. Each of them makes use of the preference of the $\mathcal{SM}$ Higgs to couple to heavy particles: either massive vector bosons (W and Z) or massive quarks (especially t-quarks). They are (see Fig. 4):

(a) gluon-gluon fusion [24],

(b) WW, ZZ fusion [25],

(c) associated production with W, Z bosons [26],

(d) associated production with $t\bar{t}$ pairs [27].

A complete review on the early literature on pp collider $\mathcal{SM}$ Higgs boson phenomenology, based on these production mechanisms, can be found in Ref. [1].

There are various uncertainties in the rates of the above processes, although none is particularly large. The most significant are: (i) the lack of precise knowledge of the gluon distribution at small x, which is important for the intermediate-mass Higgs, and (ii) the effect of unknown higher-order perturbative QCD corrections. In what follows, we will attempt to quantify the former by using recent sets of different parton distributions [10, 11, 28, 29, 30, 31] which give excellent fits to a wide range of deep inelastic scattering data (including the new structure function data from the HERA ep collider) and to data on other hard scattering processes. The latter will be estimated by studying the dependence (at next-to-leading order) of the results on the values of the renormalisation and factorisation scales.

The next-to-leading order QCD corrections are known for processes (a), (b) and (c) and are included in our calculations. By far the most important of these are the corrections to the gluon fusion process (a) which have been calculated in Ref. [32]. In the limit where the Higgs mass is far below the $2m_t$ threshold, these corrections are calculable analytically [33, 34, 35]. In fact, it turns out that the analytic result is a good approximation over the complete M_H range, and so we will use it in our analysis [36, 37]. In Ref. [37] the impact of the next-to-leading order QCD corrections for the gluon fusion process on LHC cross sections was investigated, both for the $\mathcal{SM}$ and for the $\mathcal{MSSM}$. Where our calculations overlap, we find agreement with the results of [37].

Overall, the next-to-leading order correction increases the leading-order result[7] by a factor of about 2, when the normalisation and factorisation scales are set equal to our default choice $\mu = M_H$. This 'K-factor' can be traced to a large constant piece in the next-to-leading correction [38],

$$K \approx 1 + \frac{\alpha_s(\mu = M_H)}{\pi} \left[\pi^2 + \frac{11}{2}\right]. \tag{4}$$

Such a large K-factor usually implies a non-negligible scale dependence of the theoretical cross section. We will investigate this further below.

The next-to-leading order corrections to the VV fusion [39] and VH [40] production cross sections ($V = W, Z$) are quite small, increasing the total cross sections by no more than $\approx 10\%$ (at large M_H) and $\approx 20\%$, respectively. Note that for the former we follow Ref. [39] and choose the factorisation scale to be $\mu^2 = -q_V^2$, where q_V^μ is the four-momentum of the virtual $V = W, Z$ boson. For the latter we choose $\mu^2 = \hat{s}_{pp} \approx (p_V + p_H)^2$ — the scale dependence here is in fact very weak. The corresponding QCD corrections for the $t\bar{t}H$ mechanism have not yet been computed and so we use

[7]Unless otherwise stated, here and in what follows we use 'leading-order' to denote the cross section calculated using the leading-order matrix element combined with next-to-leading order α_s and parton distributions.

the leading-order matrix elements with $\mu^2 = \hat{s}_{pp}$. A recent review of the higher-order corrections to Higgs cross sections can be found in Ref. [36].

Our results for the production cross sections are given in Figs. 5(a) and (b), for LHC energies of 10 and 14 TeV respectively. These figures can be directly compared to Fig. 6 of [3], where the cross sections were evaluated at 16 TeV. The pattern of the various curves is largely unchanged, the main differences coming from the updated input parameters and parton distributions. The gluon-gluon fusion mechanism is dominant over all the Higgs mass range, followed by WW/ZZ fusion which becomes comparable in magnitude to gluon-gluon fusion for very large Higgs masses. The cross sections of the other production mechanisms (WH, ZH and $t\bar{t}H$) are much smaller, by between one ($M_H \sim 50$ GeV) and almost three ($M_H \sim 1000$ GeV) orders of magnitude.

The values of all the cross sections at $\sqrt{s}_{pp} = 10$ and 14 TeV have of course changed with respect to their values at 16 TeV. The decrease in the cross sections between 16 TeV and 14 TeV is quite small, with a more substantial decrease between 14 TeV and 10 TeV. We quantify this in Fig. 5(c), which shows the ratio of cross sections $\sigma(10 \text{ TeV})/\sigma(14 \text{ TeV})$. The effect is largely due to the decrease in the incoming parton luminosities as higher values of momentum fraction x are probed as the overall collider energy is smaller. The effect is therefore more marked for gluon-induced processes (compare the reductions for $gg \to H$ and $q\bar{q} \to WH$), and for processes with a higher subprocess energy at the same Higgs mass (compare the reductions for $gg \to H$ and $gg \to t\bar{t}H$). For reference, the numerical values of the cross sections displayed in Figs. 5(a) and (b) are listed in Tables 1 and 2 respectively.

In early phenomenological studies, such as those of Refs. [1, 3], the uncertainty in the mass of the (as yet undiscovered) top quark provided a significant additional theoretical uncertainty in the $gg \to H$ and $gg, q\bar{q} \to t\bar{t}H$ cross sections. However, this source of uncertainty has largely disappeared: the most recent experimental measurement is $m_t = 175 \pm 6$ GeV [13], and the corresponding uncertainty on the Higgs cross sections is quite small. This is illustrated in Fig. 6, which shows the cross section ratios $\sigma(m_t = 165 \text{ GeV})/\sigma(m_t = 175 \text{ GeV})$ and $\sigma(m_t = 185 \text{ GeV})/\sigma(m_t = 175 \text{ GeV})$ for $gg \to H$ and $gg, q\bar{q} \to t\bar{t}H$ at $\sqrt{s}_{pp} = 14$ TeV. The curves have the same qualitative features as those (for $m_t = 150, 175, 200$ GeV) in Fig. 6 of Ref. [3], although the spread is of course much smaller. A lighter top quark gives a bigger cross section for $gg, q\bar{q} \to t\bar{t}H$ over essentially all of the Higgs mass range and for $gg \to H$ for $M_H \lesssim 400$ GeV. A heavier top enhances the $gg \to H$ cross section at large M_H, where the increase of the

M_H (GeV)	$\sigma(pp \to HX)$ (pb)				
	$gg \to H$	$gg, q\bar{q} \to t\bar{t}H$	$qq \to qqH$	$q\bar{q}' \to WH$	$q\bar{q} \to ZH$
50	88.	1.1	4.7	13.	6.1
100	27.	0.26	2.9	2.0	1.0
150	13.	8.2×10^{-2}	1.9	0.55	0.29
200	7.4	3.3×10^{-2}	1.3	0.20	0.11
250	5.0	1.6×10^{-2}	0.97	8.7×10^{-2}	4.7×10^{-2}
300	3.8	9.2×10^{-3}	0.71	4.3×10^{-2}	2.3×10^{-2}
350	3.7	5.9×10^{-3}	0.54	2.3×10^{-2}	1.3×10^{-2}
400	3.7	4.2×10^{-3}	0.42	1.3×10^{-2}	7.2×10^{-3}
450	2.7	3.0×10^{-3}	0.32	8.2×10^{-3}	4.3×10^{-3}
500	1.8	2.2×10^{-3}	0.26	5.2×10^{-3}	2.7×10^{-3}
550	1.2	1.7×10^{-3}	0.21	3.4×10^{-3}	1.8×10^{-3}
600	0.79	1.3×10^{-3}	0.17	2.3×10^{-3}	1.2×10^{-3}
650	0.53	1.0×10^{-3}	0.13	1.6×10^{-3}	8.1×10^{-4}
700	0.36	7.7×10^{-4}	0.11	1.1×10^{-3}	5.6×10^{-4}
750	0.25	6.1×10^{-4}	9.1×10^{-2}	7.9×10^{-4}	3.9×10^{-4}
800	0.17	4.7×10^{-4}	7.5×10^{-2}	5.7×10^{-4}	2.8×10^{-4}
850	0.12	3.6×10^{-4}	6.3×10^{-2}	4.2×10^{-4}	2.1×10^{-4}
900	8.5×10^{-2}	2.9×10^{-4}	5.2×10^{-2}	3.1×10^{-4}	1.5×10^{-4}
950	6.1×10^{-2}	2.3×10^{-4}	4.4×10^{-2}	2.3×10^{-4}	1.1×10^{-4}
1000	4.4×10^{-2}	1.9×10^{-4}	3.7×10^{-2}	1.8×10^{-4}	8.3×10^{-5}

Table 1: Higgs production cross sections for pp collisions at $\sqrt{s_{pp}} = 10$ TeV.

M_H (GeV)	$\sigma(pp \to HX)$ (pb)				
	$gg \to H$	$gg, q\bar{q} \to t\bar{t}H$	$qq \to qqH$	$q\bar{q}' \to WH$	$q\bar{q} \to ZH$
50	139.	2.6	7.8	19.	9.3
100	45.	0.60	5.1	3.1	1.6
150	23.	0.20	3.5	0.86	0.47
200	14.	8.2×10^{-2}	2.5	0.32	0.18
250	9.6	4.3×10^{-2}	1.8	0.14	8.0×10^{-2}
300	7.6	2.6×10^{-2}	1.4	7.4×10^{-2}	4.1×10^{-2}
350	7.5	1.8×10^{-2}	1.1	4.1×10^{-2}	2.2×10^{-2}
400	7.8	1.3×10^{-2}	0.87	2.4×10^{-2}	1.3×10^{-2}
450	5.8	1.0×10^{-2}	0.70	1.5×10^{-2}	8.2×10^{-3}
500	4.1	7.8×10^{-3}	0.57	9.9×10^{-3}	5.3×10^{-3}
550	2.8	6.3×10^{-3}	0.47	6.7×10^{-3}	3.6×10^{-3}
600	1.9	5.1×10^{-3}	0.39	4.7×10^{-3}	2.5×10^{-3}
650	1.3	4.0×10^{-3}	0.33	3.3×10^{-3}	1.8×10^{-3}
700	0.91	3.2×10^{-3}	0.27	2.4×10^{-3}	1.3×10^{-3}
750	0.64	2.6×10^{-3}	0.23	1.8×10^{-3}	9.2×10^{-4}
800	0.46	2.1×10^{-3}	0.20	1.3×10^{-3}	6.9×10^{-4}
850	0.33	1.7×10^{-3}	0.17	1.0×10^{-3}	5.2×10^{-4}
900	0.24	1.4×10^{-3}	0.15	7.8×10^{-4}	3.9×10^{-4}
950	0.18	1.2×10^{-3}	0.13	6.0×10^{-4}	3.0×10^{-4}
1000	0.13	9.6×10^{-4}	0.11	4.7×10^{-4}	2.3×10^{-4}

Table 2: Higgs production cross sections for pp collisions at $\sqrt{s}_{pp} = 14$ TeV.

$t\bar{t}H$ coupling is the dominant factor. For very heavy Higgs bosons, the cross section increases by about 30% as m_t increases from 165 to 185 GeV. If we assume that by the time the LHC comes into operation the top quark mass will be known with a precision of ± 5 GeV or better, then the residual uncertainty in the Higgs production cross section will be less than $\pm O(10\%)$.

Since a large part of the uncertainties on the Higgs cross sections at the LHC stems from the small x behaviour of the gluon distributions[8], Fig. 7 shows the total rates for the $gg \to H$ process at $\sqrt{s}_{pp} = 14$ TeV for 11 different sets of parton distributions: MRS(A) [10], MRS(A′), MRS(G) [30], MRS(R1,R2) [11], CTEQ2M, CTEQ2MS, CTEQ2MF, CTEQ2ML, CTEQ3M [28] and GRV94HO [29]. Evidently, a band of $\pm 20\%$ centred on the MRS(A) calculation covers the various cross section predictions. Fig. 8 shows the corresponding gluon distributions for the same parton sets used in Fig. 7, in the x range spanned by intermediate- and heavy-mass Higgs production, and at the characteristic factorisation scale $Q = x\sqrt{s}_{pp}$.

There are two main factors which influence the differences between the various predictions shown in Fig. 7: the shape of the gluon distribution at medium and small x, and the value of α_s associated with each parton set. The majority of parton sets in Fig. 7 use the traditional 'DIS' α_s value, i.e. $\alpha_s(M_Z) \simeq 0.113$. For such sets, the differences in the cross sections come mainly from the shape of the starting gluon distribution. Thus the sets MRS(A,A′) and CTEQ3M yield similar predictions, being fitted to similar data sets under similar assumptions. The gluons of sets MRS(G) and GRV94HO have significantly steeper gluons (see Fig. 8), and hence give larger Higgs cross sections at small M_H. In fact, both these gluons have recently been shown to be in disagreement with the the latest HERA data [11]. Note also that the CTEQ2Mx sets of partons give generally small Higgs cross sections due to smaller gluons at small x. These too are disfavoured by the latest HERA data.

The most recent partons shown in Fig. 7 are the sets MRS(R1) amd MRS(R2). The former are effectively the successors to the MRS(A,A′) partons, and give similar Higgs cross sections. For MRS(R1), $\alpha_s(M_Z) = 0.113$ which is slightly larger than the value for MRS(A,A′). In addition, the starting gluon for MRS(R1)is also slightly larger than that for MRS(A′) (see Fig. 5(a) of Ref. [11]). These two effects combine to give a MRS(R1) Higgs cross section which is between 5% and 10% larger than that of MRS(A). More interesting is the prediction for the MRS(R2) partons. For this set $\alpha_s(M_Z) = 0.120$.

[8]For a simple fusion process like $gg \to H$, the parton x value is typically $x \sim M_H/\sqrt{s}_{pp}$.

This larger value is more in line with the LEP $e^+e^- \to$hadrons/jets determinations, and also with the CDF and D0 large E_T jet data (for a full discussion see Ref. [11]). The effect on the Higgs cross section is very noticeable, see Fig. 7. The MRS(R2) cross section is some 10−15% larger than that of MRS(R1), consistent with the difference between the values of α_s^2 corresponding to each set.

It should of course be remembered that by the time the LHC comes into operation, the uncertainty on the gluon distribution at medium and small x may be expected to be significantly smaller, principally due to improved measurements of the small-x deep-inelastic structure functions at HERA, and of large p_T jet and prompt photon production at the Tevatron $p\bar{p}$ collider (see for example Refs. [30, 11]). The apparent 'disagreement' between the DIS and LEP α_s values will also presumably be resolved. At the present time, we may say that the $\pm 20\%$ spread around the MRS(A) prediction in Fig. 7 constitutes a conservative estimate of the uncertainty on the Higgs cross section predictions due to parton distributions.[9]

As already mentioned, the dominant $gg \to H$ process has a large next-to-leading order correction, which leads to a non-negligible scale dependence. Fig. 9 shows the dependence at lowest and higher order of the Higgs production cross section in the gluon-gluon channel on the (equal) renormalisation and factorisation scales μ, e.g., for $\sqrt{s} = 14$ TeV, $M_H = 100$ GeV and $m_t = 175$ GeV. To make a consistent analysis, we have plotted the rates obtained by using, on the one hand (continuous line), NLO amplitude formulae, NLO parton distributions (i.e. GRV94HO) and α_s computed at two loops and, on the other hand (dashed line), the LO matrix element, LO structure functions (i.e. GRV94LO) and strong coupling constant evolved at one loop. We use the GRV94 sets of parton distributions in order to allow for a more straightforward comparison of our results with the corresponding ones given in Ref. [37], although one should notice that in Ref. [37] the old GRV92 set [41] was used, so that this might be in the end a source of small differences. As can be seen from the figure, the (unphysical) variation of the cross section with the two scales is largely reduced at higher order, as expected. If μ is varied (conservatively) between $M_H/4$ and $4M_H$, the rates at NLO decrease by a factor 1.54, whereas at LO the ratio is 1.93. Furthermore, we have repeated the calculations presented in Ref. [37], using $M_H = 150$ and 500 GeV (and also, for consistency, $m_t = 174$ GeV). Our results exhibit the same pattern recognised

[9] The parton distribution uncertainty on the sub-dominant quark-induced Higgs cross sections, e.g. $qq \to qqH$, is of course much smaller, as the quark distributions are pinned down rather precisely by DIS structure function data.

there. That is, the improvement in scale stability gained at next-to-leading order is more significant for large Higgs masses. However, we find that our NLO rates are typically more sensitive to the value of μ than those given in Ref. [37] (although by only a few percent, in general). We believe that this difference originates in our use of the analytical formulae obtained in the heavy top approximation $M_H^2/4m_t^2 \ll 1$, whereas in Ref. [37] the exact (numerical) results were presented. In fact, we know that the scale dependence at NLO of approximated results is a delicate issue, since in several instances these have been found to be more sensitive to the choice of μ that those at LO (see, for example, Ref. [35])[10]. Note that lowering the collider energy slightly enhances the μ-dependence of the cross sections. For example, at 10 TeV the numbers corresponding to the two ratios mentioned above are 1.60 (NLO) and 2.08 (LO), respectively.

Next, we multiply the production cross sections by the branching ratios of Section 3 to obtain event rates for various channels. Considering all the possible combinations of production mechanisms and decay channels [4, 5], the best chance of discovering a $\mathcal{SM}$ Higgs at the LHC appears to be given by the following signatures: (i) $gg \to H \to \gamma\gamma$, (ii) $q\bar{q}' \to WH \to \ell\nu_\ell\gamma\gamma$[11] and (iii) $gg \to H \to Z^{(*)}Z^{(*)} \to \ell^+\ell^-\ell'^+\ell'^-$, where $\ell, \ell' = e$ or μ. Recently, the importance of several other modes has been emphasised. By exploiting techniques of flavour identification of b-jets, thereby reducing the huge QCD background from light-quark and gluon jets, the modes (iv) $q\bar{q}' \to WH \to \ell\nu_\ell b\bar{b}$ and (v) $gg, q\bar{q} \to t\bar{t}H \to b\bar{b}b\bar{b}WW \to b\bar{b}b\bar{b}\ell\nu_\ell X$, can be used to search for the $\mathcal{SM}$ Higgs [42, 43]. Another potentially important channel, particularly for the mass range $2M_W \lesssim M_H \lesssim 2M_Z$, is (vi) $H \to W^{(*)}W^{(*)} \to \ell^+\nu_\ell\ell'^-\bar{\nu}_{\ell'}$ [44]. Here the lack of a measurable narrow resonant peak is compensated by a relatively large branching ratio, since for this mass range $H \to WW$ is the dominant decay mode.

In Figs. 10–14 we show the product of the cross sections and branching ratios for the above channels, again at 10 and 14 TeV, for the Higgs mass ranges where they give sizeable event rates (in Figs. 11(b) and 12(b) m_t is set equal to 175 GeV). As already noticed in Ref. [3], the combination of a rising $H \to \gamma\gamma$ branching ratio with a falling cross section yields, for cases (i) and (ii) above, a remarkably constant signal for $M_H \lesssim 140$ GeV.

[10] Indeed we have been able to reproduce the trend of some of the results given in Ref. [35].

[11] In principle we should also include $q\bar{q} \to ZH \to \ell^+\ell^-\gamma\gamma$, although a very high luminosity would be needed to make this detectable.

Finally, we should also mention the channel: (vii) $H \to ZZ \to \ell\bar{\ell}\nu\bar{\nu}$, with $\ell = e, \mu$ and e, μ, τ-neutrinos, since it may offer additional chances for Higgs detection in the very heavy mass range [4, 5].[12] The corresponding event rates can be obtained simply by multiplying the numbers of Fig. 13a–b by six.

5 Conclusions

In this paper we have computed all the decay modes and the most important production mechanisms of the $\mathcal{SM}$ Higgs at the LHC, by using the most recent sets of parton distributions and by including in our computations all the available next-to-leading order corrections. Cross sections have been presented for two values of the LHC collider energy, $\sqrt{s_{pp}} = 10$ and 14 TeV. As the most promising signatures which should allow for Higgs detection at the LHC are

- $gg \to H \to \gamma\gamma$,
- $q\bar{q}' \to WH \to \ell\nu_\ell\gamma\gamma$ and $gg, q\bar{q} \to t\bar{t}H \to \ell\nu_\ell\gamma\gamma X$,
- $q\bar{q}' \to WH \to \ell\nu_\ell b\bar{b}$ and $gg, q\bar{q} \to t\bar{t}H \to b\bar{b}b\bar{b}WW \to b\bar{b}b\bar{b}\ell\nu_\ell X$,
- $gg \to H \to Z^{(*)}Z^{(*)} \to \ell^+\ell^-\ell'^+\ell'^-$, where $\ell, \ell' = e$ or μ,
- $gg \to H \to W^{(*)}W^{(*)} \to \ell^+\nu_\ell\ell'^-\bar{\nu}_{\ell'}$, where $\ell, \ell' = e$ or μ,[13]
- $gg \to H \to ZZ \to \ell^+\ell^-\nu_{\ell'}\bar{\nu}_{\ell'}$, where $\ell = e$ or μ and $\ell' = e, \mu$ or τ,

we have presented updated numbers for the corresponding event rates. The theoretical uncertainty of the results, which mainly arises from

- the lack of precise knowledge of the gluon distribution at small x (which is particularly important for the intermediate mass Higgs case, the most difficult to recognise at the LHC),
- the uncertainty in the value of $\alpha_s(M_Z)$,

[12] When the Higgs resonance becomes very broad, for large $M(H)$, the $p_T(Z \to \ell\bar{\ell})$ spectrum may give a cleaner signal.

[13] In the analysis of Ref. [44] the additional decay channels $W \to \tau\nu \to (e, \mu) + \nu$'s were also included, yielding a slightly larger signal event rate.

- the effect of unknown higher-order perturbative QCD corrections as well as the scale dependence of those already computed,

has been investigated and estimated, by adopting different sets of recent NLO parton distributions and comparing their results, and by studying the (renormalisation and factorisation) scale dependence, at NLO, of the most important Higgs production channel (via gluon-gluon fusion) at the LHC. We estimate the current theoretical errors to be $\approx \pm 20\%$ (for the uncertainty due to parton distributions and α_s) and $\approx \pm 30\%$ (for the error due to the scale dependence, see also Ref. [37]), the latter for the gluon-gluon fusion process.

In summary, the values presented here for branching ratios, cross sections and event rates correspond to the state-of-the-art in our current knowledge of the input quantities and higher-order corrections, and should be a useful reference for the normalisations used in the various experimental simulations.

Acknowledgements

We thank Michael Spira for useful comments and suggestions. SM and WJS are grateful to the UK PPARC for support. This work was supported in part by the EU Programme "Human Capital and Mobility", Network "Physics at High Energy Colliders", contract CHRX-CT93-0537 (DG 12 COMA).

Note added. After submitting this manuscript to the journal we received a private communication from Michael Spira in which he confirmed the correctness of our speculation about the discrepancies between the approximate analytical result and the numerical complete one in the scale dependence of the $gg \to H$ cross sections at NLO [45].

References

[1] J.F. Gunion, H.E. Haber, G.L. Kane and S. Dawson, *"The Higgs Hunter Guide"* (Addison-Wesley, Reading MA, 1990).

[2] Proceedings of the "*Large Hadron Collider Workshop*", Aachen, 4-9 October 1990, eds. G. Jarlskog and D. Rein, Report CERN 90-10, ECFA 90-133, Geneva, 1990.

[3] Z. Kunszt and W.J. Stirling, in Ref. [2].

[4] ATLAS Technical Proposal, CERN/LHC/94-43 LHCC/P2 (December 1994).

[5] CMS Technical Proposal, CERN/LHC/94-43 LHCC/P1 (December 1994).

[6] W.J. Marciano, *Phys. Rev.* **D29** (1984) 580.

[7] S.G. Gorishny, A.L. Kataev, S.A. Larin and L.R. Surguladze, *Mod. Phys. Lett.* **A5** (1990) 2703;
L.R. Surguladze, *Phys. Lett.* **B341** (1994) 60.

[8] T. Inami, T. Kubota and Y. Okada, Z. Phys. **C18** (1983) 69;
H. Zheng and D. Wu, *Phys. Rev.* **D42** (1990) 3760;
A. Djouadi, M. Spira, J.J. van der Bij and P.M. Zerwas, *Phys. Lett.* **B257** (1991) 187;
A. Djouadi, M. Spira and P.M. Zerwas, *Phys. Lett.* **B276** (1992) 350;
S. Dawson and R.P. Kauffman, *Phys. Rev.* **D47** (1993) 1264.

[9] M. Djouadi, M. Spira and P.M. Zerwas, *Phys. Lett.* **B264** (1991) 440.

[10] A.D. Martin, R.G. Roberts and W.J. Stirling, *Phys. Rev.* **D50** (1994) 6734.

[11] A.D. Martin, R.G. Roberts and W.J. Stirling, *Phys. Lett.* **B387** (1996) 419.

[12] J.H. Kühn, *Act. Phys. Pol.* **B12** (1981) 347;
J.H. Kühn, *Act. Phys. Austr. Suppl.* **XXIV** (1982) 203.

[13] P. Grannis, presented at the ICHEP96 Conference, Warsaw (1996).

[14] B. Kniehl, DESY Report No. 93-069, August 1993 (to appear in *Phys. Rep.*); "*Higher-order corrections to Higgs-boson Decays*", to appear in the Proceedings of the "*1994 Zeuthen Workshop on Elementary Particle Theory: Physics at LEP 200 and Beyond*", Teupitz, Germany, April 10-15, 1994, eds. J. Blümlein and T. Riemann (to be published in *Nucl. Phys.* **B** *Proceedings Supplements*).

[15] M. Carena, P.M. Zerwas *et al.*, "*Higgs Physics*" in "Physics at LEP2", eds. G. Altarelli, T. Sjöstrand and F. Zwirner, CERN Report 96-01, Vol.1, p.351 (1996).

[16] W.-Y. Keung and W.J. Marciano, *Phys. Rev.* **D30** (1984) 248;
R.N. Cahn, *Rep. Prog. Phys.* **52** (1989) 389.

[17] A. Barroso, J. Pulido and J.C. Romão, *Nucl. Phys.* **B267** (1986) 509;
A. Barroso and J.C. Romão, *Nucl. Phys.* **B272** (1986) 693.

[18] A. Grau, G. Pancheri and R.J.N. Phillips, *Phys. Lett.* **B251** (1990) 293.

[19] K. Melnikov, M. Spira and O. Yakovlev, *Z. Phys.* **C64** (1994) 401.

[20] A. Djouadi, M. Spira and P.M. Zerwas, *Phys. Lett.* **B311** (1993) 255;
K. Melnikov and O. Yakovlev, *Phys. Lett.* **B312** (1993) 179;
M. Spira, *preprint* DESY 95-073, April 1995, presented at the Ringsberg Workshop on Electromagnetic Interactions, Ringsberg, Germany, Feb 5-9, 1995;
D. Graudenz, *preprint* CERN-TH/95-77, C95-03-19, March 1995, talk given at 30th Rencontres de Moriond: QCD and High Energy Hadronic Interactions, Meribel les Allues, France, 19-25 March 1995;
M. Spira, A. Djouadi, D. Graudenz and P.M. Zerwas, *Nucl. Phys.* **B453** (1995) 17.

[21] S. Moretti and W.J. Stirling, *Phys. Lett.* **B347** (1995) 291; Erratum, *ibidem* **B366** (1996) 451.

[22] A. Djouadi, M. Spira and P.M. Zerwas, in Refs. [20];
M. Spira, A. Djouadi, D. Graudenz and P.M. Zerwas, in Refs. [20].

[23] M. Spira, private communication.

[24] H. Georgi, S.L. Glashow, M.E. Macahek and D.V. Nanopoulos, *Phys. Rev. Lett.* **40** (1978) 692.

[25] R.N. Cahn and S. Dawson, *Phys. Lett.* **B136** (1984) 196.

[26] S.L. Glashow, D.V. Nanopoulos and A. Yildiz, *Phys. Rev.* **D18** (1978) 1724;
Z. Kunszt, Z. Trocsanyi and W.J. Stirling, *Phys. Lett.* **B271** (1991) 247.

[27] Z. Kunszt, *Nucl. Phys.* **B247** (1984) 339;
J.F. Gunion, *Phys. Lett.* **B253** (1991) 269;
W.J. Marciano and F.E. Paige, *Phys. Rev. Lett.* **66** (1991) 2433;
J.F. Gunion, H.E. Haber, F.E. Paige, W.-K. Tung and S.S.D. Willenbrock, *Nucl. Phys.* **B294** (1987) 621;
D.A. Dicus and S.S.D. Willenbrock, *Phys. Rev.* **D39** (1989) 751.

[28] H.L. Lai, J. Botts, J. Huston, J.G. Morfin, J.F. Owens, J. Qiu, W.K. Tung and H. Weerts, *Phys. Rev.* **D51** (1995) 4763.

[29] M. Gluck, E. Reya and A. Vogt, *Z. Phys.* **C67** (1995) 433.

[30] A.D. Martin, R.G. Roberts and W.J. Stirling, *Phys. Lett.* **B354** (1995) 155.

[31] A.D. Martin, R.G. Roberts and W.J. Stirling, *Phys. Lett.* **B356** (1995) 89.

[32] D. Graudenz, M. Spira and P.M. Zerwas, *Phys. Rev. Lett.* **70** (1993) 1372.

[33] A. Djouadi, M. Spira and P.M. Zerwas, in Ref. [9].

[34] S. Dawson, *Nucl. Phys.* **B359** (1991) 283.

[35] S. Dawson and R.P. Kauffman, *Phys. Rev.* **D49** (1993) 2298.

[36] A. Djouadi, *Int. J. Mod. Phys.* **A10** (1995) 1;
A. Djouadi, *preprint* UdeM-GPP-TH-04 (1994), Talk given at 16th Annual MRST (Montreal-Rochester-Syracuse-Toronto) Meeting on High Energy Physics: What Next? Exploring the Future of High Energy Physics, Montreal, Canada, 12-13 May 1994.

[37] M. Spira, A. Djouadi, D. Graudenz and P.M. Zerwas, in Ref. [20].

[38] D. Graudenz, M. Spira and P.M. Zerwas, in Ref. [32].

[39] T. Han, G. Valencia and S. Willenbrock, *Phys. Rev. Lett.* **69** (1992) 3274.

[40] T. Han and S. Willenbrock, *Phys. Lett.* **B273** (1991) 167.

[41] M. Glück, E. Reya and A. Vogt, *Z. Phys.* **C53** (1992) 127.

[42] A. Stange, W. Marciano and S. Willenbrock, *Phys. Rev.* **D49** (1994) 1354; *Phys. Rev.* **D50** (1994) 4491.

[43] J.F. Gunion and T. Han, *Phys. Rev.* **D51** (1995) 1051.

[44] M. Dittmar and H. Dreiner, *preprint* RAL-96-049 (1996), hep-ph/9608317.

[45] M. Spira, *preprint* DESY-T-95-05, October 1995.

Figure captions

[1] Branching ratios of the $\mathcal{SM}$ Higgs boson in the mass range 50 GeV $< M_H <$ 200 GeV, for the decay modes: a) $b\bar{b}$, $c\bar{c}$, $\tau^+\tau^-$, $\mu^+\mu^-$ and gg; b) WW, ZZ, $\gamma\gamma$ and $Z\gamma$.

[2] Branching ratios of the $\mathcal{SM}$ Higgs boson in the mass range 200 GeV $< M_H <$ 1 TeV, for the decay modes: WW, ZZ and $t\bar{t}$ ($m_t = 175$ GeV).

[3] Total width of the $\mathcal{SM}$ Higgs as a function of the mass in the range 50 GeV $< M_H <$ 1 TeV ($m_t = 175$ GeV).

[4] Representative Feynman diagrams describing the main mechanisms of Higgs production at the LHC: (a) gluon-gluon fusion; (b) WW- or ZZ-fusion; (c) associated production with W or Z; and (d) associated production with top quark pairs.

[5] Total cross sections for H production at the LHC as a function of the Higgs mass M_H, as given by the four production mechanisms illustrated in Fig. 4, at $\sqrt{s}_{pp} = 10$ TeV (a) and $\sqrt{s}_{pp} = 14$ TeV (b), and their ratios $\sigma(10\ \mathrm{TeV})/\sigma(14\ \mathrm{TeV})$ (c). Here, $m_t = 175$ GeV.

[6] The ratios R_t of the total cross sections for H production, via $gg \to H$ (continuous curves) and $gg, q\bar{q} \to t\bar{t}H$ (dashed curves), as a function of the Higgs mass M_H, at $\sqrt{s}_{pp} = 10$ and 14 TeV, for $m_t = 165$ and 175 GeV, and for $m_t = 185$ and 175 GeV.

[7] Ratios (with respect to MRS(A)) of $\mathcal{SM}$ Higgs production cross sections from gluon-gluon fusion calculated using eleven different sets of parton distributions: MRS(A, A$'$, G, R1, R2), CTEQ(2M, 2MS, 2MF, 2ML, 3M) and GRVHO94. Note that $m_t = 175$ GeV.

[8] Behaviour of the gluon distributions $xg(x, Q^2)$ of the various parton sets used in Fig. 7 as a function of x, with $Q^2 = x^2 s_{pp}$ and $\sqrt{s}_{pp} = 14$ TeV. The ordering of the labels in the legend corresponds to increasing values of xg at the minimum value of x.

[9] Higgs production cross section for $\sqrt{s} = 14$ TeV, $M_H = 100$ GeV from the gluon-gluon fusion process, as a function of the (equal) renormalisation and factorisation

scales μ, at LO and NLO order. The GRV94 sets have been used here. Note that $m_t = 175$ GeV.

[10] Total cross sections for $\mathcal{SM}$ Higgs production times the branching ratio for the decay mode $H \to \gamma\gamma$, as a function of the Higgs mass M_H in the low mass range, at $\sqrt{s}_{pp} = 10$ TeV and $\sqrt{s}_{pp} = 14$ TeV.

[11] Total cross sections for WH (continuous curves) and ZH production (dashed curves) (a) and for $t\bar{t}H$ (continuous curves) (b) times the branching ratios of the decay modes $H \to \gamma\gamma$, $W \to \ell\nu_\ell$, $Z \to \ell^+\ell^-$ and $t\bar{t} \to \ell\nu_\ell X$ ($\ell = e, \mu$), as a function of the Higgs mass M_H in the low mass range, at $\sqrt{s}_{pp} = 10$ TeV and $\sqrt{s}_{pp} = 14$ TeV. Note that $m_t = 175$ GeV.

[12] Total cross sections for WH and ZH production (a) and for $t\bar{t}H$ (b) times the branching ratios of the decay modes $H \to b\bar{b}$, $W \to \ell\nu_\ell$, $Z \to \ell^+\ell^-$ and $t\bar{t} \to \ell\nu_\ell X$ ($\ell = e, \mu$), as a function of the Higgs mass M_H in the low mass range, at $\sqrt{s}_{pp} = 10$ TeV and $\sqrt{s}_{pp} = 14$ TeV. Note that $m_t = 175$ GeV.

[13] Total cross sections for $\mathcal{SM}$ Higgs production times the branching ratio for the decay mode $H \to Z^{(*)}Z^{(*)} \to \ell^+\ell^-\ell^+\ell^-$ ($\ell = e, \mu$), as a function of the Higgs mass in the ranges (a) 50 GeV $\leq M_H \leq$ 300 GeV and (b) 100 GeV $\leq M_H \leq$ 1 TeV, at $\sqrt{s}_{pp} = 10$ TeV and $\sqrt{s}_{pp} = 14$ TeV. Note that $m_t = 175$ GeV.

[14] Total cross sections for $\mathcal{SM}$ Higgs production times the branching ratio for the decay mode $H \to W^{(*)}W^{(*)} \to \ell^+\nu_\ell\ell'^-\bar{\nu}_{\ell'}$ ($\ell, \ell' = e, \mu$), as a function of the Higgs mass in the range $0 \leq M_H \leq 300$ GeV, at $\sqrt{s}_{pp} = 10$ TeV and $\sqrt{s}_{pp} = 14$ TeV. Note that $m_t = 175$ GeV.

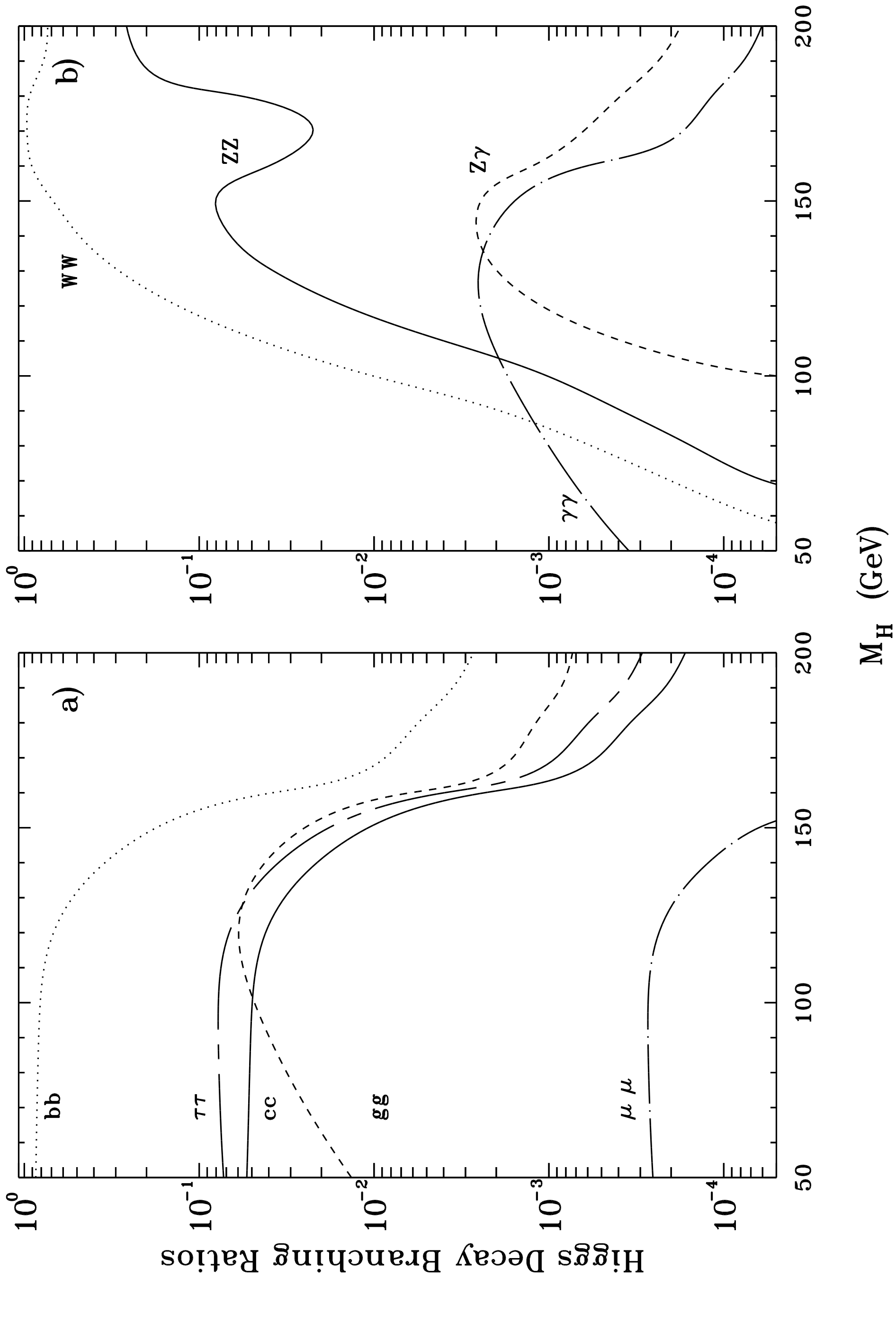
Higgs Decay Branching Ratios
a)
b)
bb
ττ
cc
gg
μ μ
WW
ZZ
Zγ
γγ
M_H (GeV)

Fig. 1

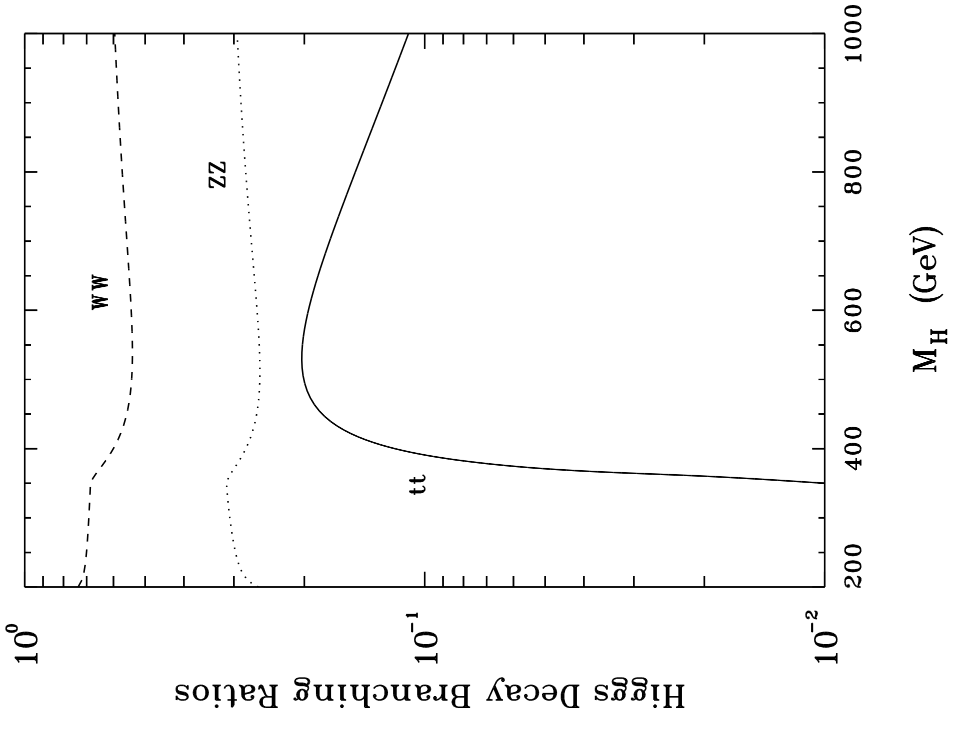

Higgs Decay Branching Ratios
10^0
10^{-1}
10^{-2}
200
400
600
800
1000
WW
ZZ
tt
M_H (GeV)

Fig. 2

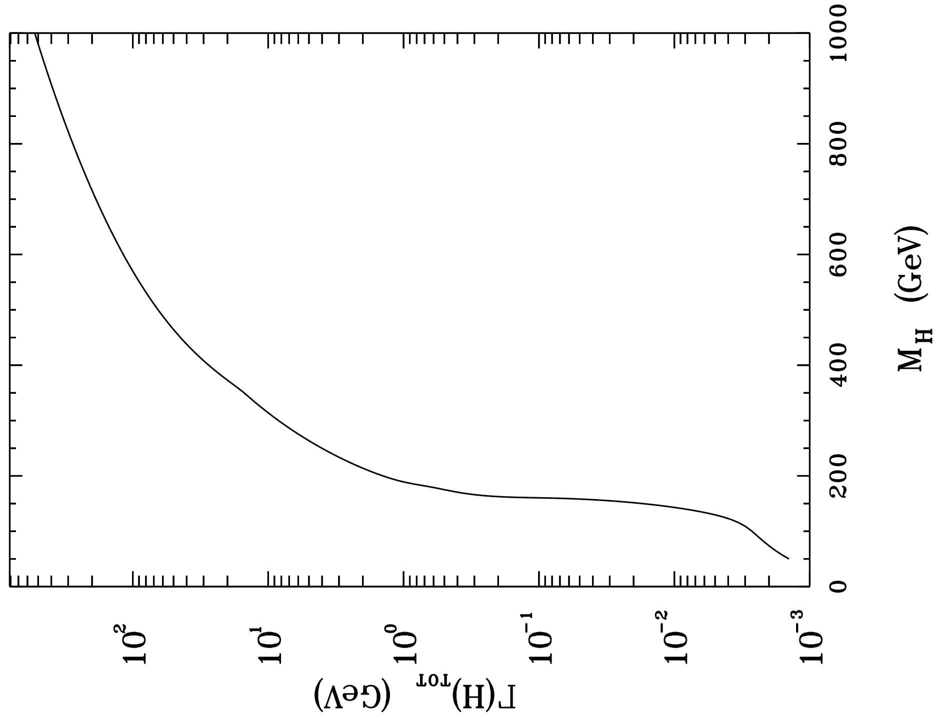

$\Gamma(H)_{TOT}$ (GeV)
10^2
10^1
10^0
10^{-1}
10^{-2}
10^{-3}
0
200
400
600
800
1000
M_H (GeV)

Fig. 3

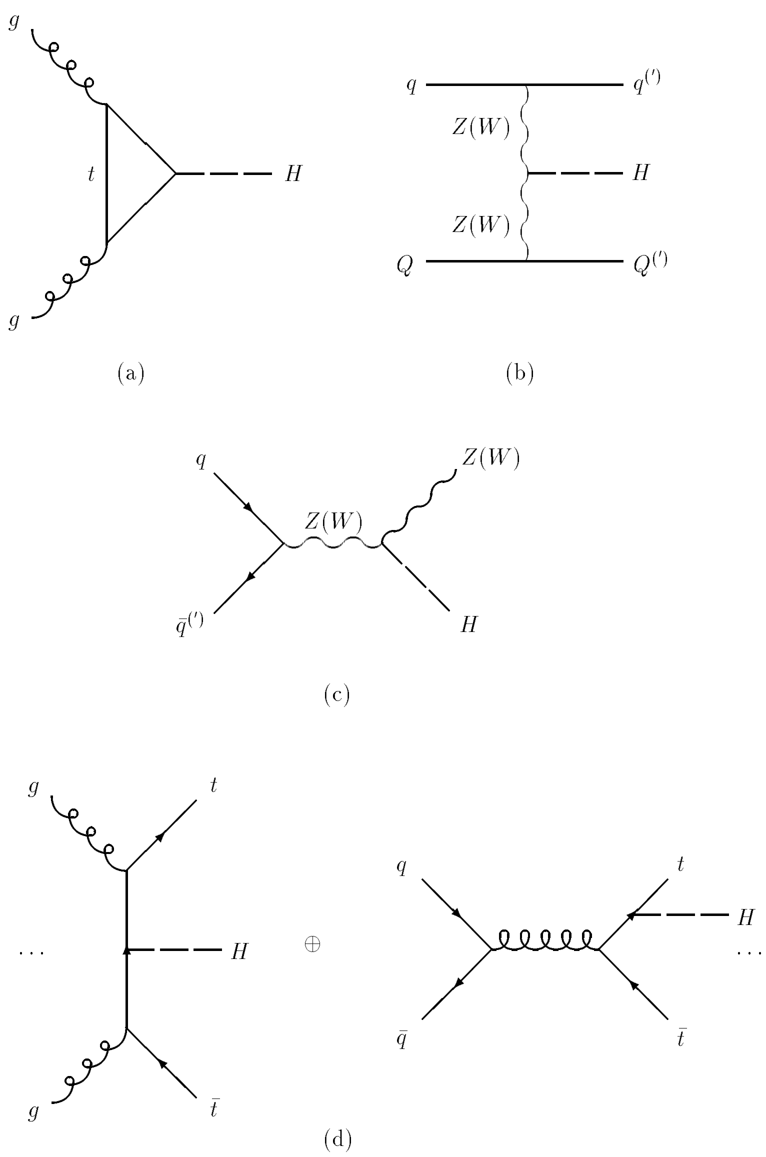

Fig. 4

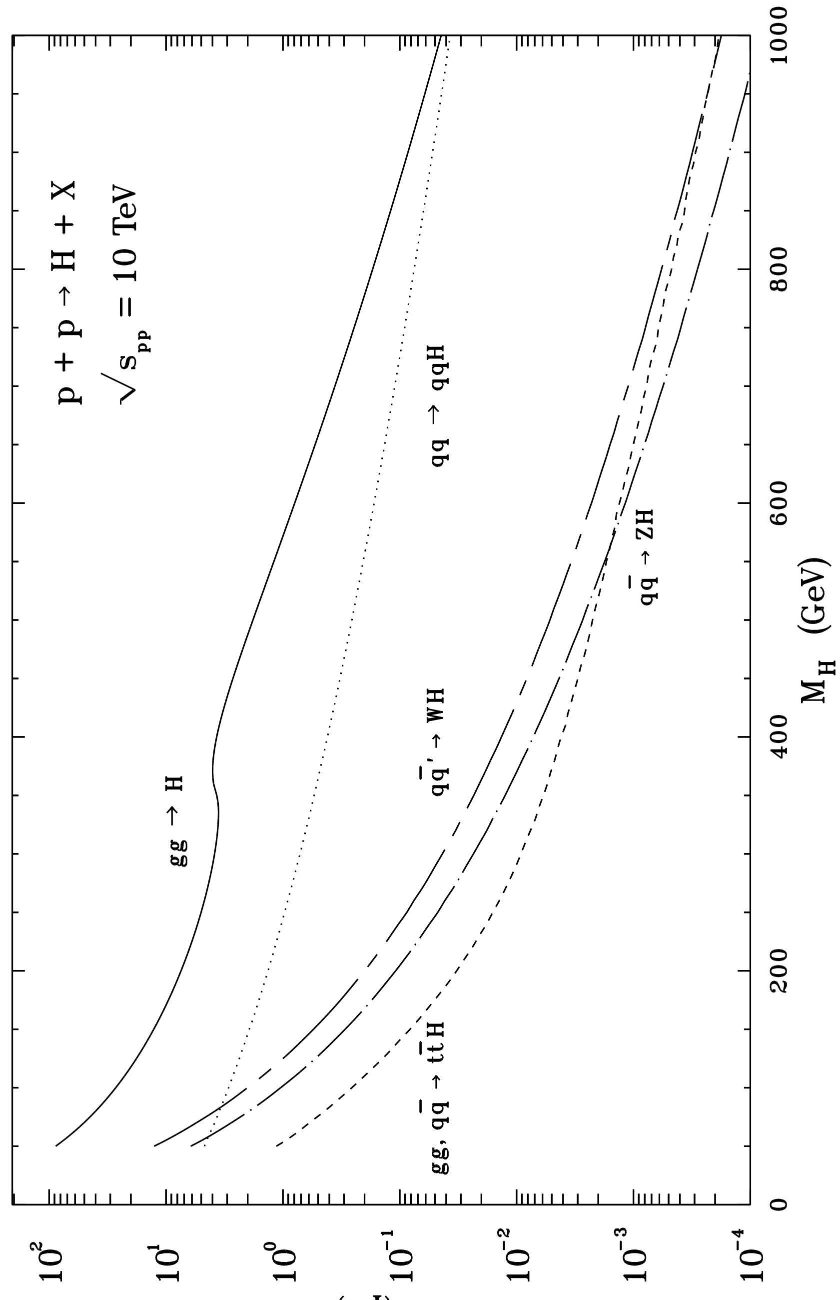

$p + p \to H + X$
$\sqrt{s_{pp}} = 10$ TeV
σ (pb)
10^{2}
10^{1}
10^{0}
10^{-1}
10^{-2}
10^{-3}
10^{-4}
0
200
400
600
800
1000
M_H (GeV)
$gg \to H$
$qq \to qqH$
$q\bar{q}' \to WH$
$q\bar{q} \to ZH$
$gg, q\bar{q} \to t\bar{t}H$

Fig. 5a

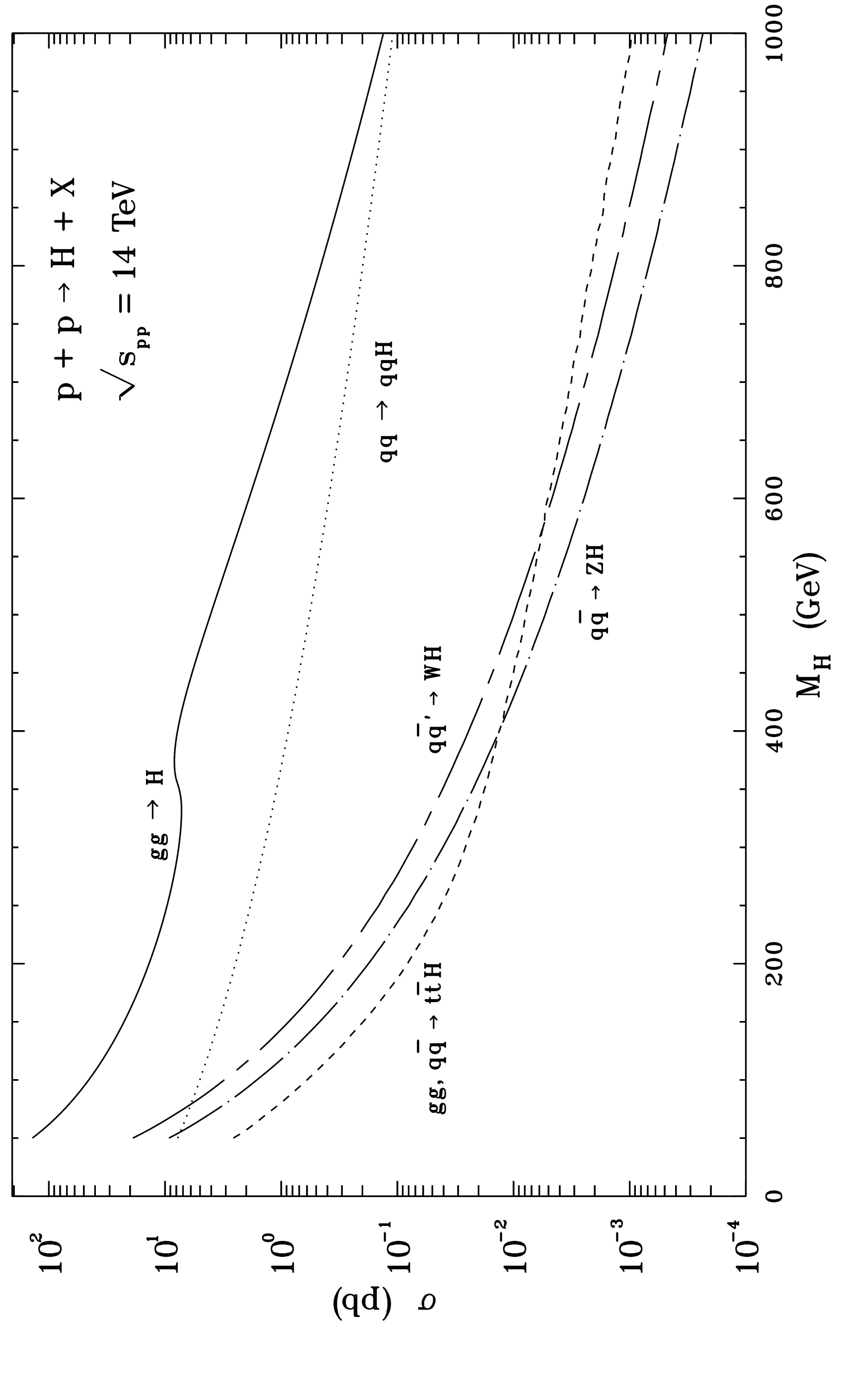
p + p → H + X
$\sqrt{s_{pp}}$ = 14 TeV
gg → H
qq → qqH
$q\bar{q}'$ → WH
$q\bar{q}$ → ZH
gg, $q\bar{q}$ → $t\bar{t}$H
σ (pb)
M_H (GeV)
10^{2}
10^{1}
10^{0}
10^{-1}
10^{-2}
10^{-3}
10^{-4}
0
200
400
600
800
1000

Fig. 5b

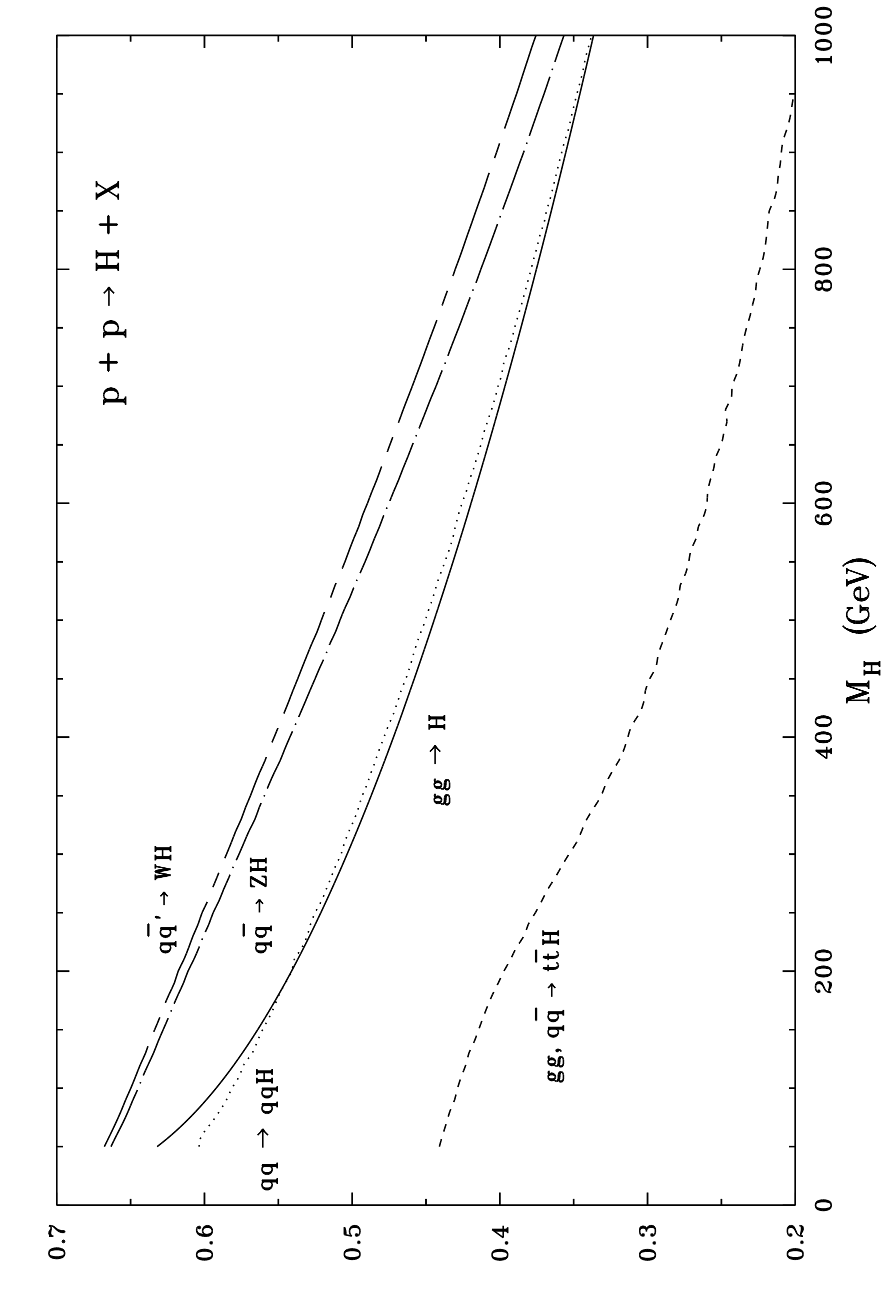
p + p → H + X
$q\bar{q}' \to WH$
$q\bar{q} \to ZH$
$gg \to H$
$qq \to qqH$
$gg, q\bar{q} \to t\bar{t}H$
M_H (GeV)
σ(10 TeV)/σ(14 TeV)
0
200
400
600
800
1000
0.2
0.3
0.4
0.5
0.6
0.7

Fig. 5c

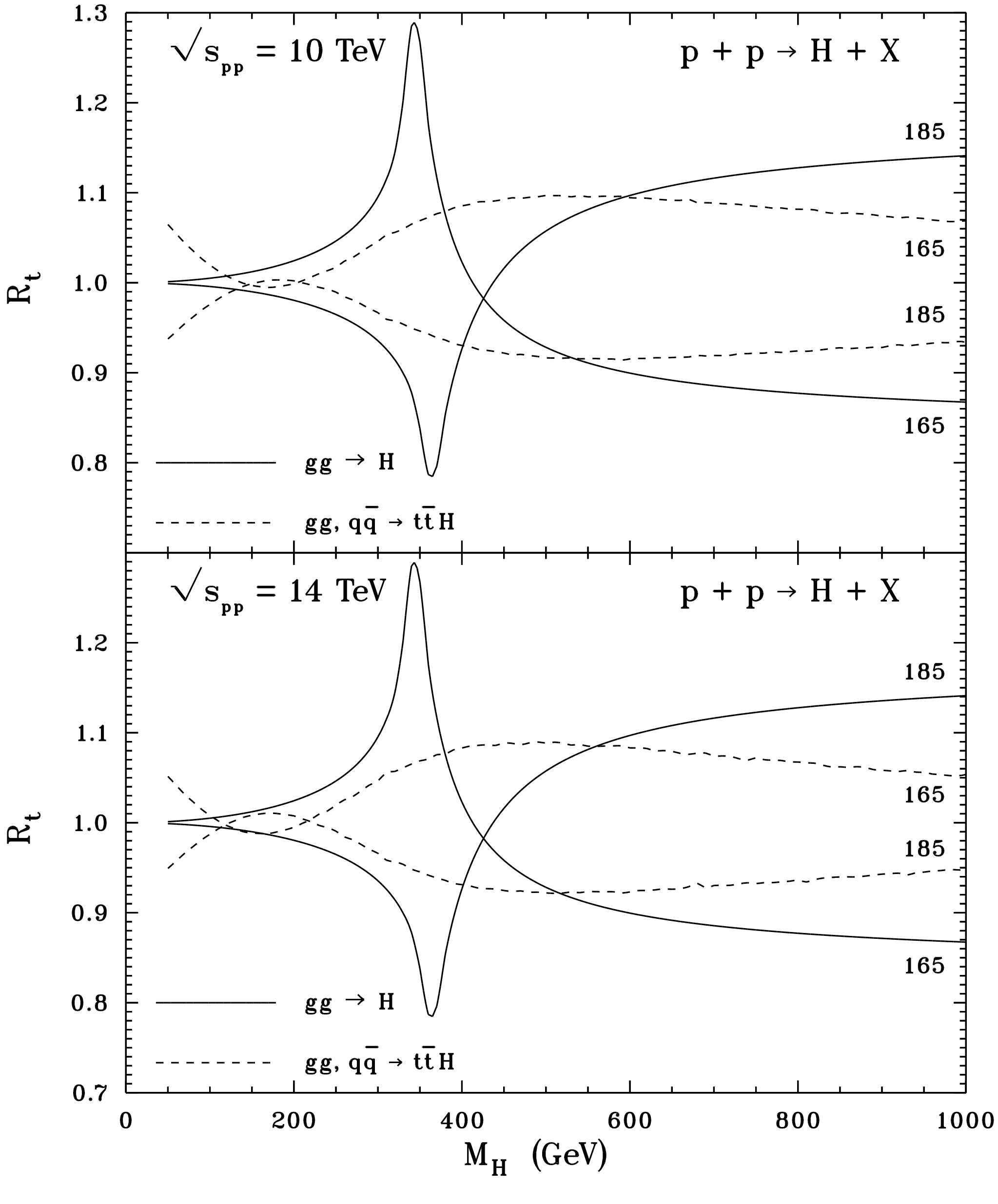

$\sqrt{s_{pp}}$ = 10 TeV
p + p → H + X
185
165
185
165
gg → H
gg, $q\bar{q}$ → $t\bar{t}$H
$\sqrt{s_{pp}}$ = 14 TeV
p + p → H + X
185
165
185
165
gg → H
gg, $q\bar{q}$ → $t\bar{t}$H
R_t
M_H (GeV)
0
200
400
600
800
1000
0.7
0.8
0.9
1.0
1.1
1.2
1.3

Fig. 6

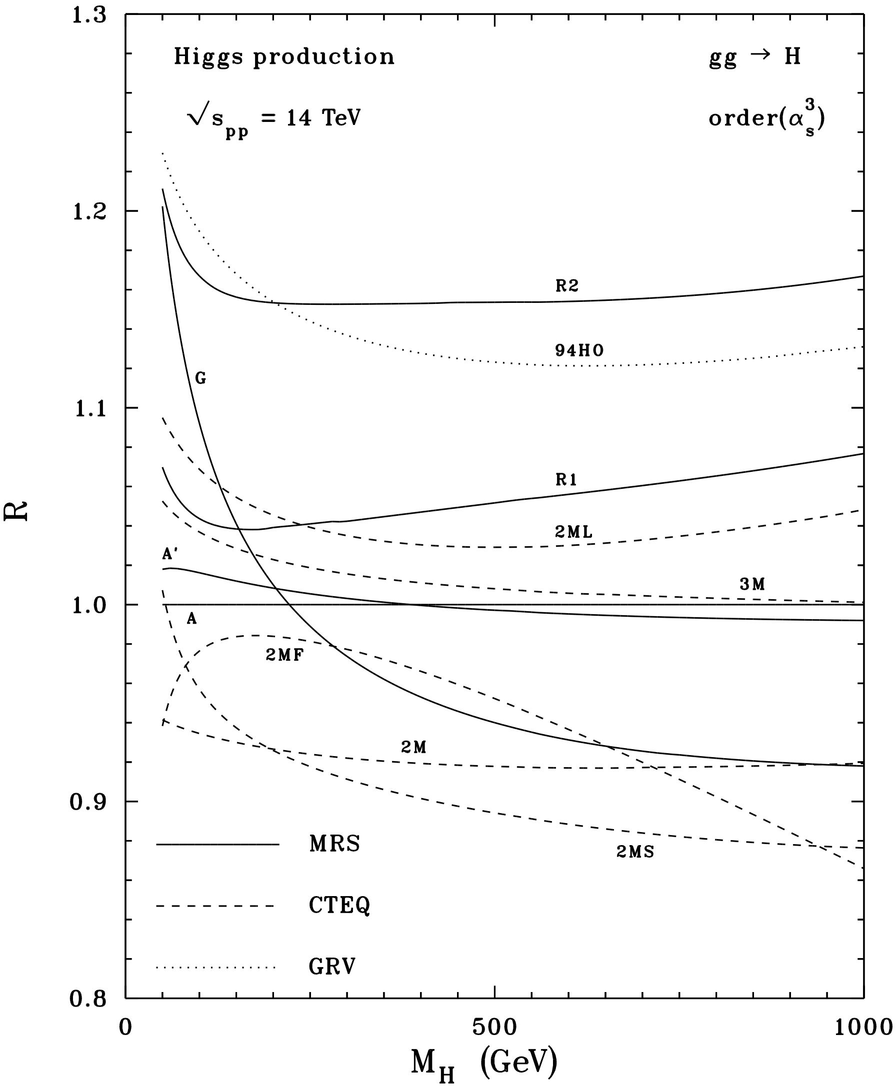

Higgs production
gg → H
$\sqrt{s_{pp}}$ = 14 TeV
order(α_s^3)
R2
94HO
G
R1
2ML
A'
3M
A
2MF
2M
2MS
MRS
CTEQ
GRV
1.3
1.2
1.1
1.0
0.9
0.8
R
0
500
1000
M_H (GeV)

Fig. 7

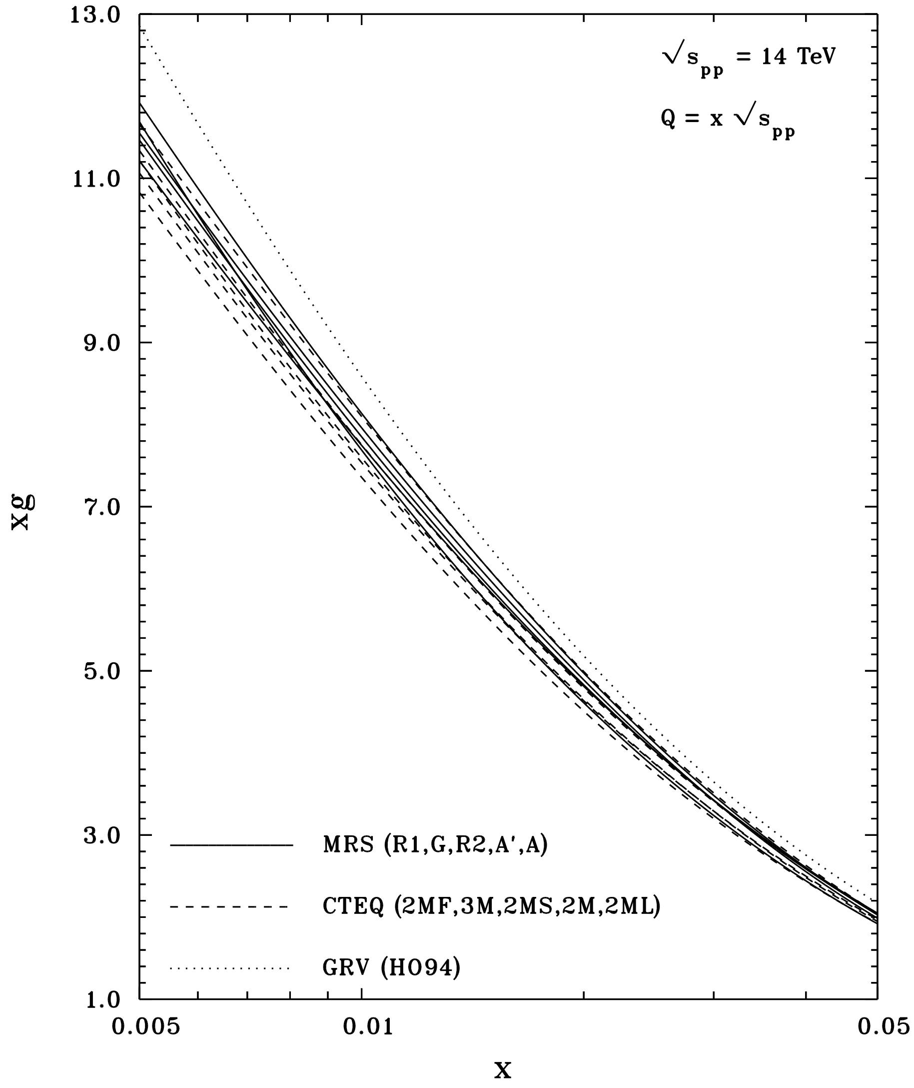

13.0
11.0
9.0
7.0
5.0
3.0
1.0
xg
0.005
0.01
0.05
x
$\sqrt{s_{pp}}$ = 14 TeV
Q = x $\sqrt{s_{pp}}$
MRS (R1,G,R2,A',A)
CTEQ (2MF,3M,2MS,2M,2ML)
GRV (HO94)

Fig. 8

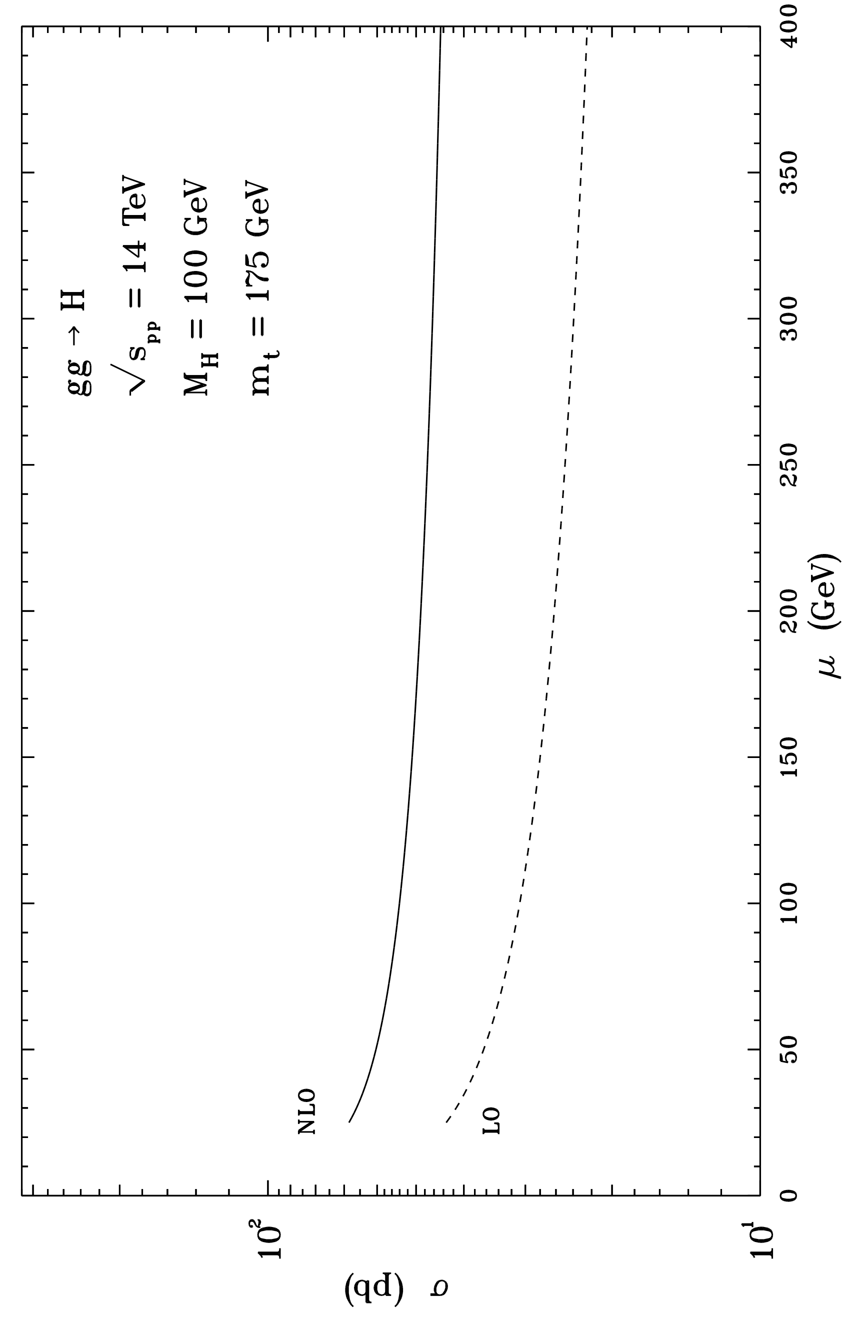

$gg \to H$
$\sqrt{s_{pp}} = 14$ TeV
$M_H = 100$ GeV
$m_t = 175$ GeV
NLO
LO
σ (pb)
10^2
10^1
0
50
100
150
200
250
300
350
400
μ (GeV)

Fig. 9

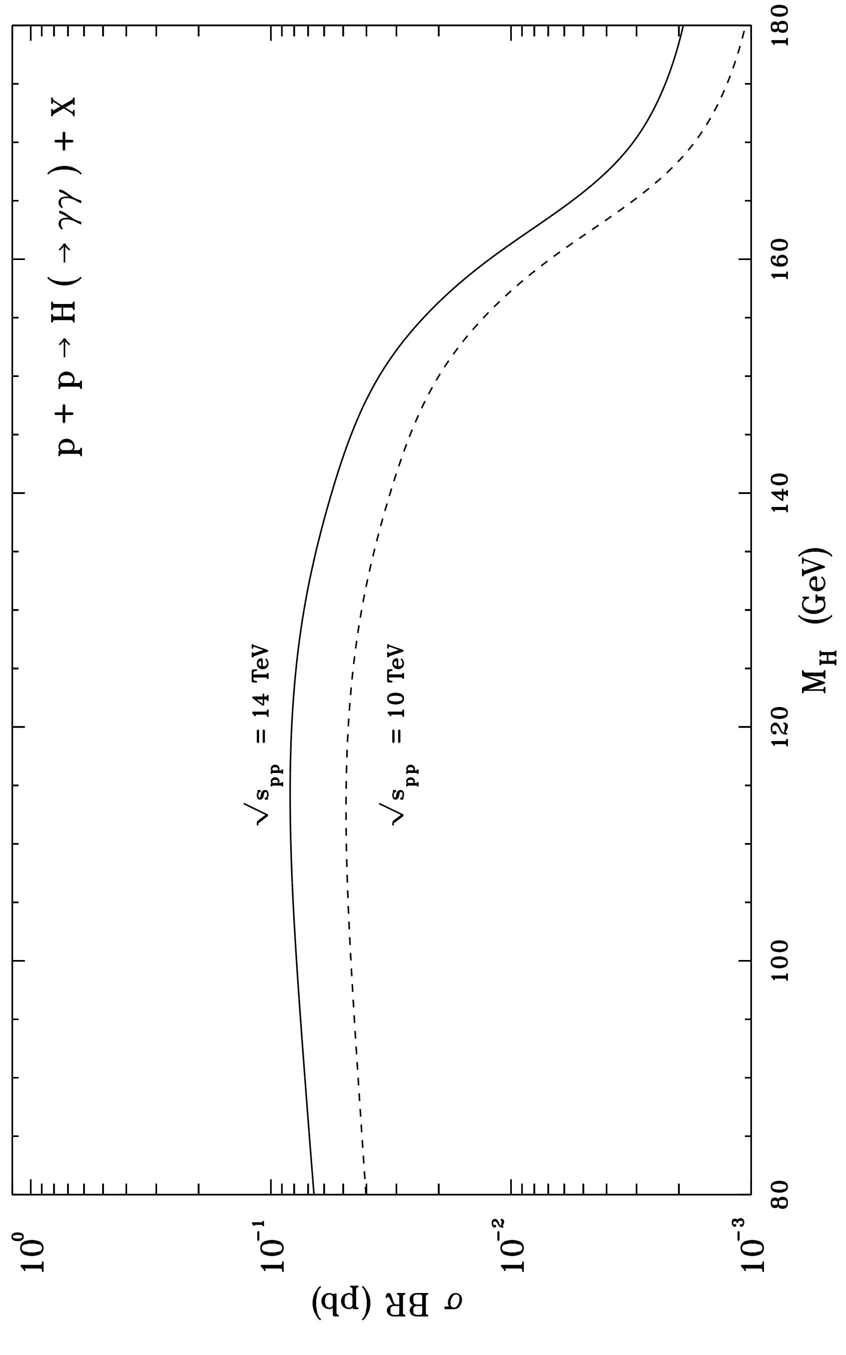

p + p → H (→ γγ) + X
√s_pp = 14 TeV
√s_pp = 10 TeV
σ BR (pb)
M_H (GeV)
10^0
10^-1
10^-2
10^-3
80
100
120
140
160
180

Fig. 10

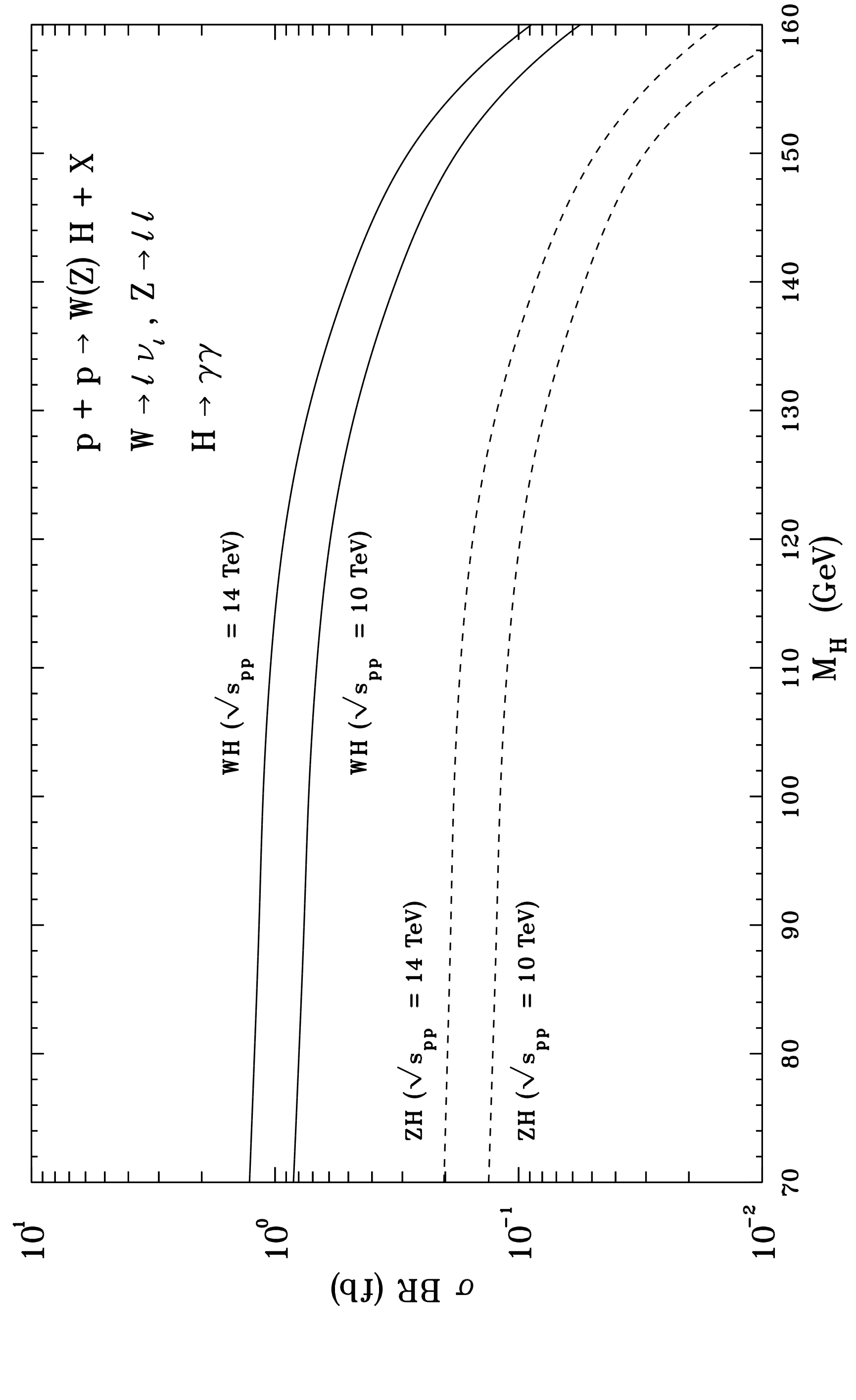

p + p → W(Z) H + X
W → ℓ ν_ℓ , Z → ℓ ℓ
H → γγ
WH (√s_pp = 14 TeV)
WH (√s_pp = 10 TeV)
ZH (√s_pp = 14 TeV)
ZH (√s_pp = 10 TeV)
σ BR (fb)
M_H (GeV)
10^1
10^0
10^-1
10^-2
70
80
90
100
110
120
130
140
150
160

Fig. 11a

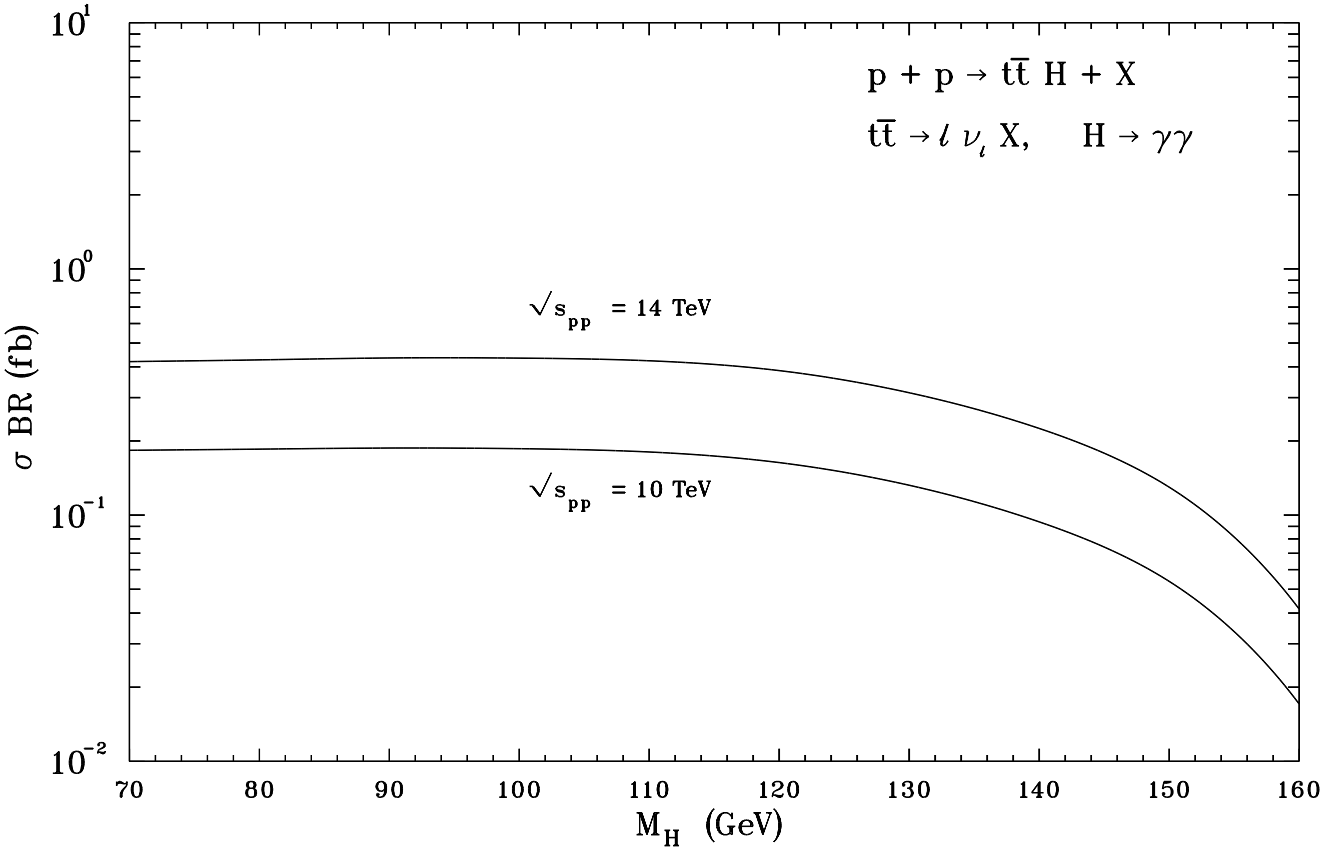

p + p → t$\bar{t}$ H + X
t$\bar{t}$ → ℓ ν_ℓ X,   H → γγ
$\sqrt{s_{pp}}$ = 14 TeV
$\sqrt{s_{pp}}$ = 10 TeV
σ BR (fb)
10^{1}
10^{0}
10^{-1}
10^{-2}
70
80
90
100
110
120
130
140
150
160
M_H (GeV)

Fig. 11b

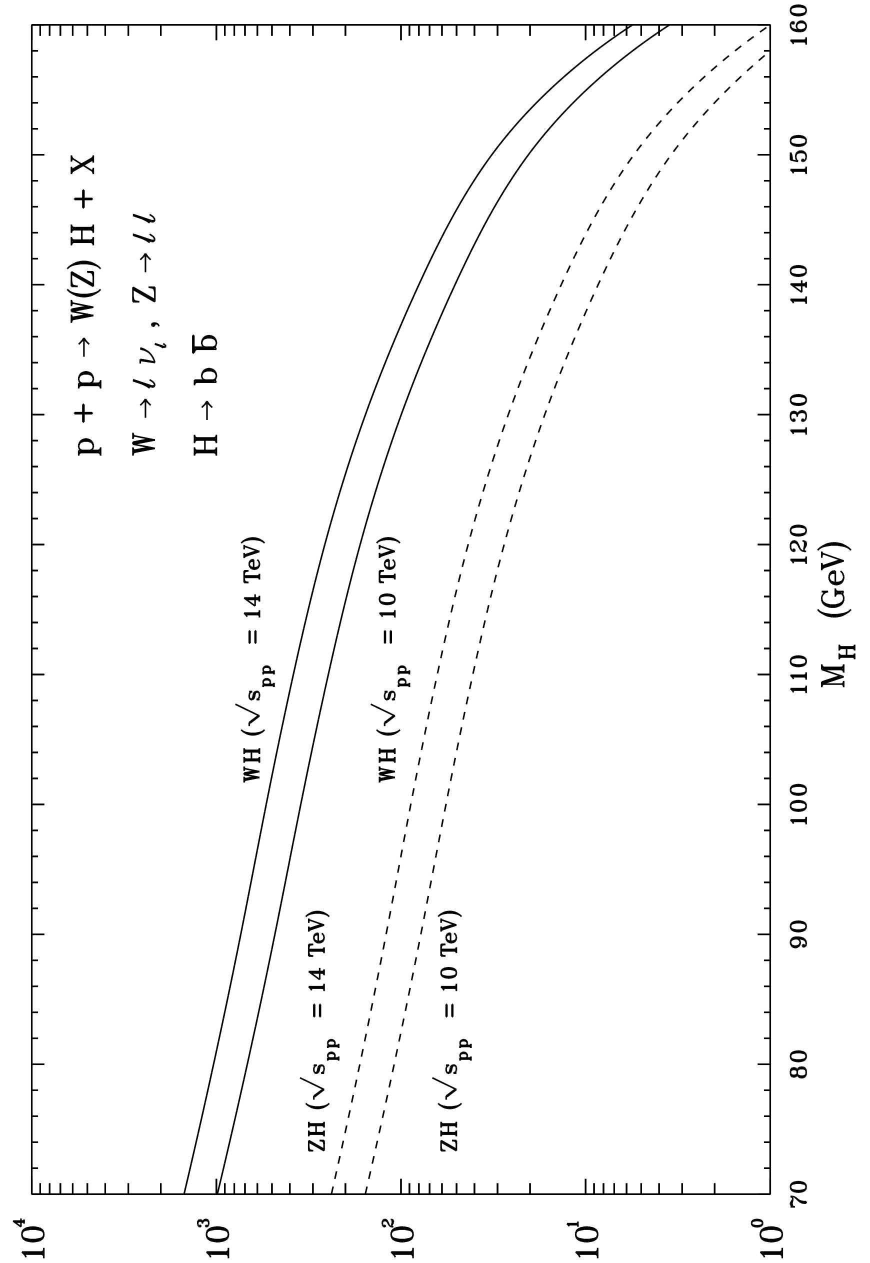

p + p → W(Z) H + X
W → ℓ ν_ℓ , Z → ℓ ℓ
H → b b̄
WH (√s_pp = 14 TeV)
WH (√s_pp = 10 TeV)
ZH (√s_pp = 14 TeV)
ZH (√s_pp = 10 TeV)
σ BR (fb)
M_H (GeV)
10^4
10^3
10^2
10^1
10^0
70
80
90
100
110
120
130
140
150
160

Fig. 12a

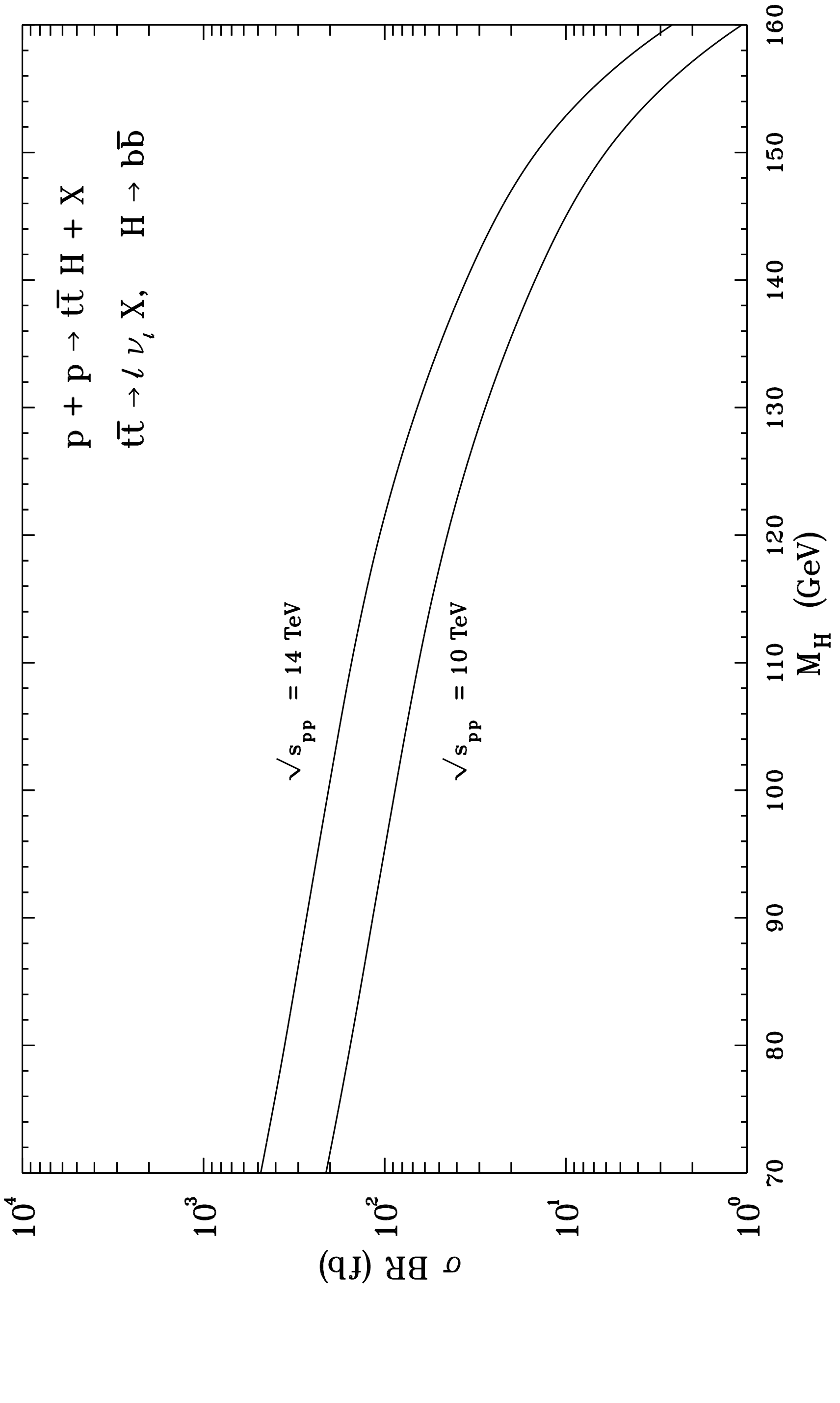
p + p → $t\bar{t}$ H + X
$t\bar{t} \to \ell\, \nu_\ell$ X,   H → $b\bar{b}$
$\sqrt{s_{pp}}$ = 14 TeV
$\sqrt{s_{pp}}$ = 10 TeV
M_H (GeV)
σ BR (fb)
70
80
90
100
110
120
130
140
150
160
10^0
10^1
10^2
10^3
10^4

Fig. 12b

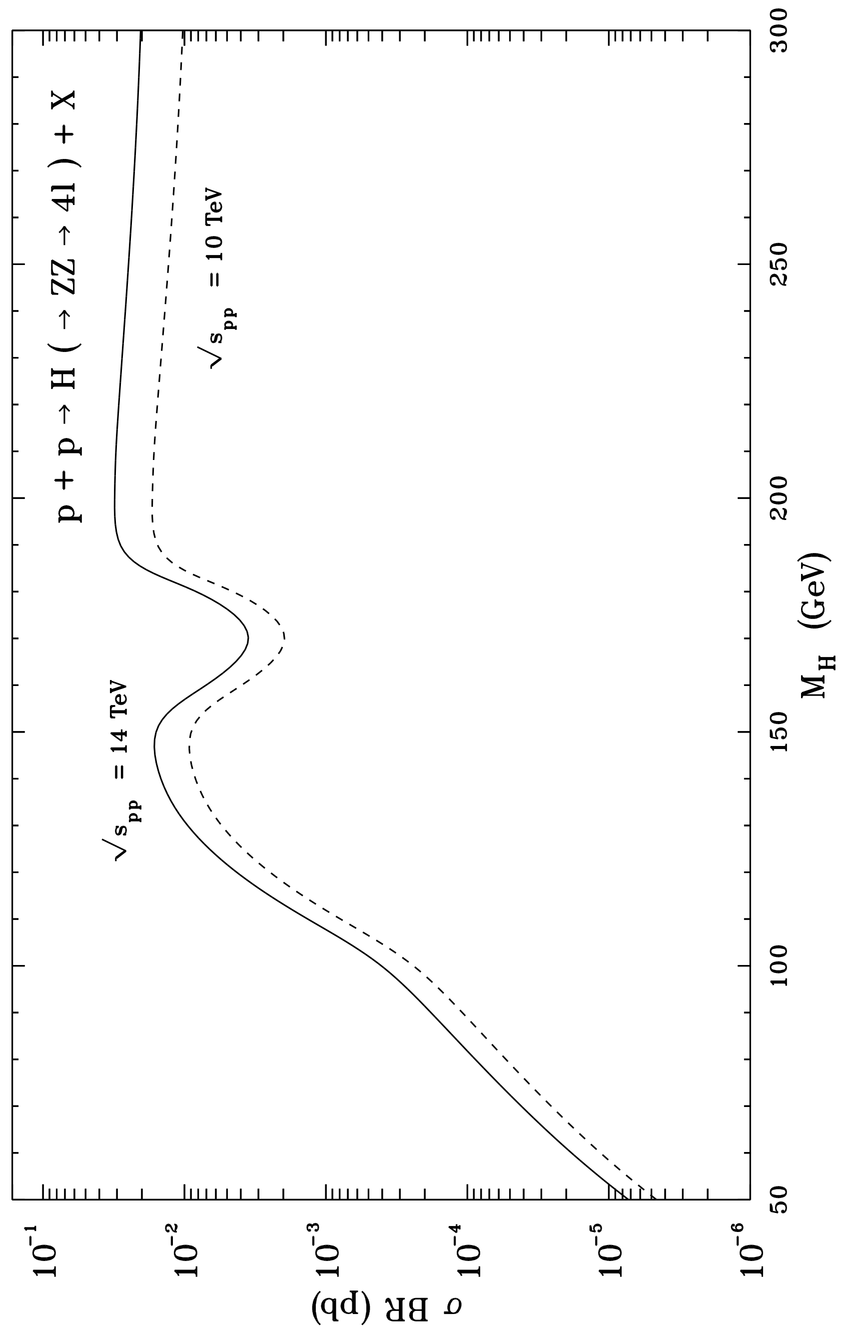

p + p → H (→ ZZ → 4l) + X
√s_pp = 14 TeV
√s_pp = 10 TeV
σ BR (pb)
M_H (GeV)
10^-1
10^-2
10^-3
10^-4
10^-5
10^-6
50
100
150
200
250
300

Fig. 13a

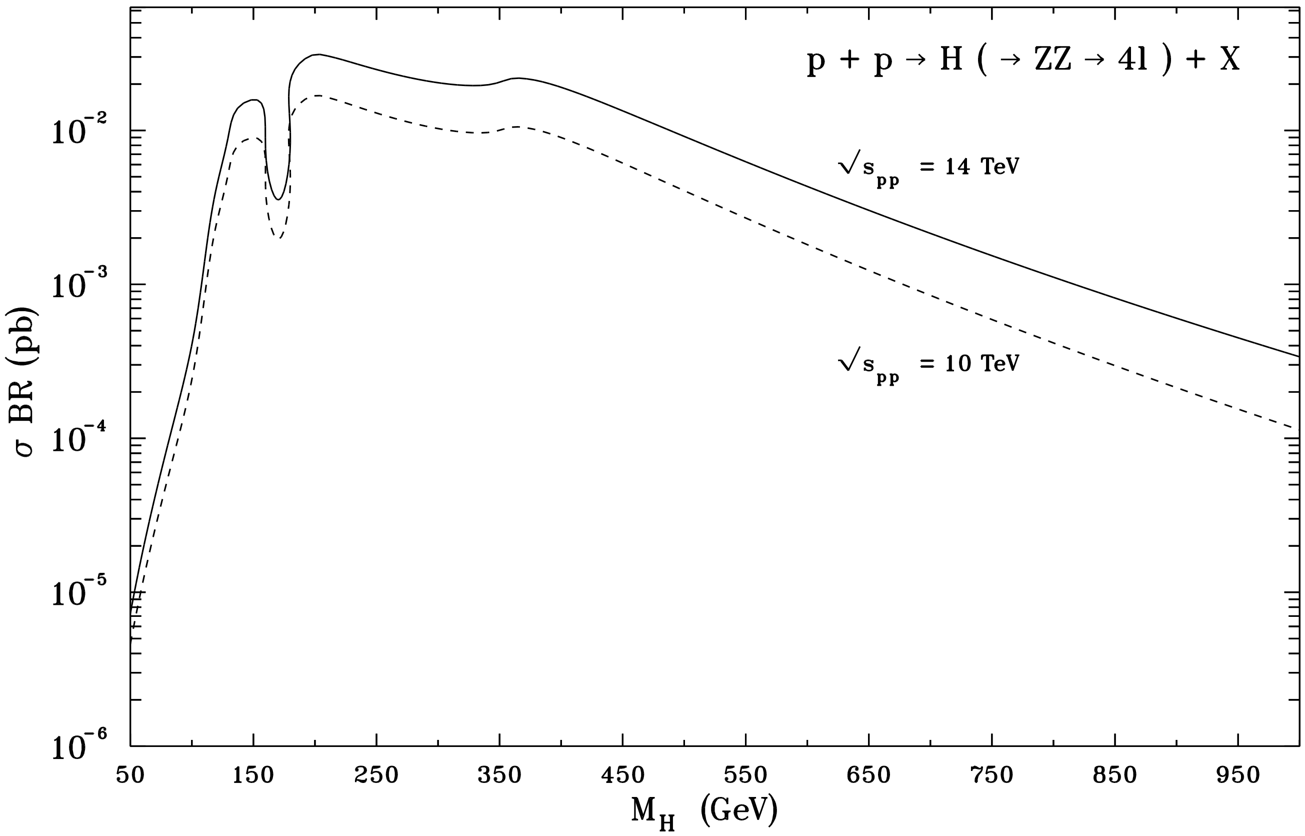

p + p → H (→ ZZ → 4l) + X
$\sqrt{s_{pp}}$ = 14 TeV
$\sqrt{s_{pp}}$ = 10 TeV
σ BR (pb)
10^{-2}
10^{-3}
10^{-4}
10^{-5}
10^{-6}
50 150 250 350 450 550 650 750 850 950
M_H (GeV)

Fig. 13b

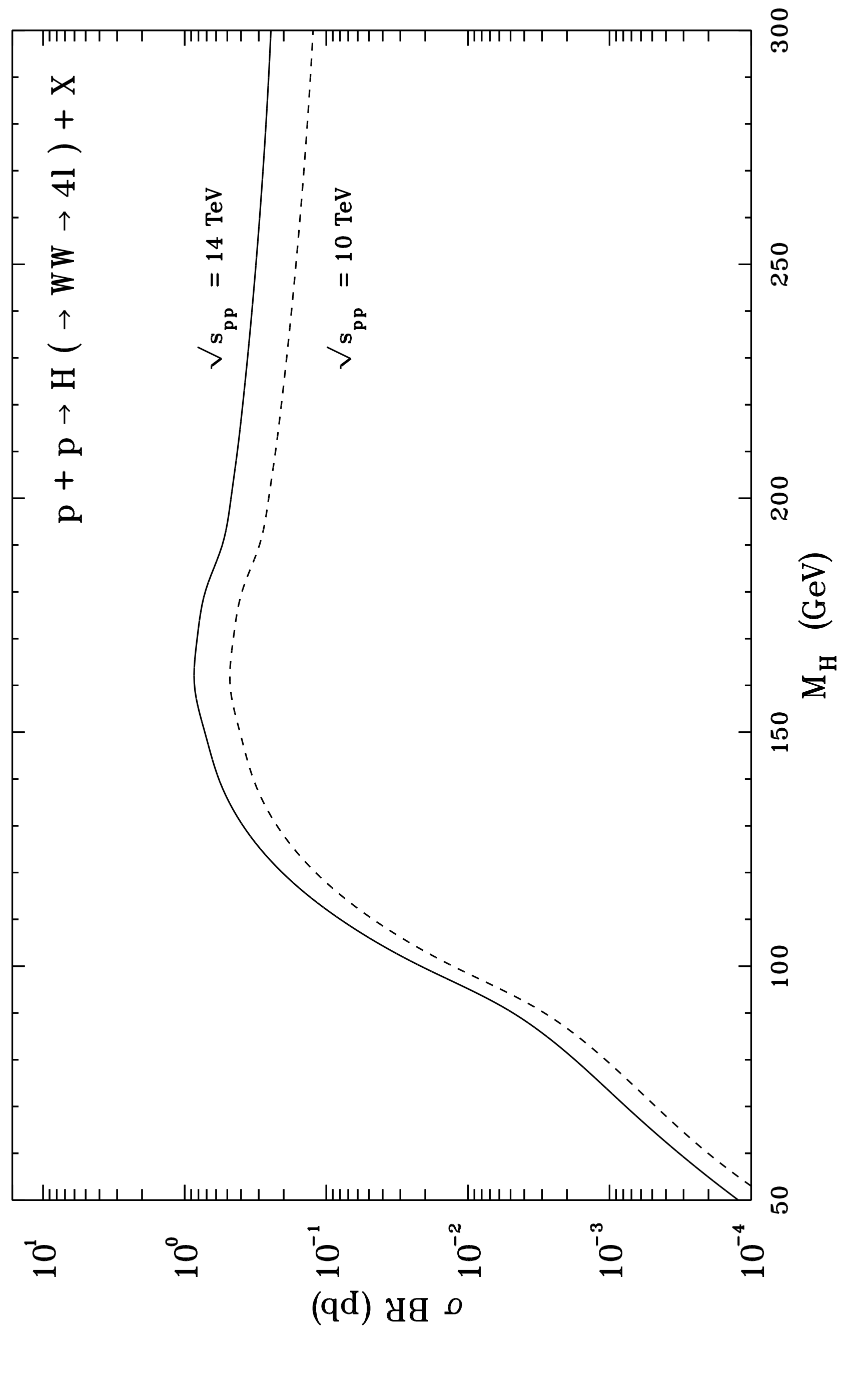
p + p → H (→ WW → 4l) + X
$\sqrt{s_{pp}}$ = 14 TeV
$\sqrt{s_{pp}}$ = 10 TeV
σ BR (pb)
10^{1}
10^{0}
10^{-1}
10^{-2}
10^{-3}
10^{-4}
50
100
150
200
250
300
M_H (GeV)

Fig. 14